

# Exact Schwarzian Metric Factor and Holographic Wilson-Loop Screening

Miguel Tierz

Shanghai Institute for Mathematics and Interdisciplinary Sciences (SIMIS),  
Block A, No. 657 Songhu Road, Yangpu District, Shanghai 200438, China

tierz@simis.cn

July 7, 2026

## Abstract

We evaluate exactly the radial metric factor  $h(\zeta)$  generated by Schwarzian averaging in the  $\text{AdS}_2$  throat of an extremal Reissner–Nordström  $\text{AdS}_5$  black brane. The result is a Gaussian integral against  $\coth(\pi y)$ , valid at all radial depths, which Mordell’s identity turns into an exact Appell–Lerch  $q/q^*$ -series representation. The dual series identifies the nonperturbative scale  $e^{-\pi^2 C/\zeta}$  missed by any finite near-boundary truncation. The third parametric derivative required by the evaluation generates the quasimodular Eisenstein series  $E_2$ , absent from the classical Mordell identity. From the integral representation we prove that  $\mathcal{G}_0(\zeta) := h(\zeta)/\zeta^2$  is completely monotone and hence has no interior minimum, so any confining minimum produced by a finite near-boundary truncation is an artifact. We also compute the exact relative variance of the Schwarzian kernel, which makes the averaged-metric approximation error quantitative and shows that the absence of a confining minimum is robust across moment-based effective geometries. Applied to the temporal rectangular Wilson loop, the exact throat gives algebraic screening,  $E(L) \sim -\kappa_{\text{IR}}/L^2$ , the Wilson-loop diagnostic of the semi-local quantum-liquid IR of the extremal RN brane. A numerical check in a simple matched geometry confirms that the screened saddle is the dominant string configuration, and an exact-versus-truncated force comparison shows that the apparent constant-force regime of the fourth-order truncation is not a feature of the exact geometry.

## Contents

<b>1</b>	<b>Introduction</b>	<b>2</b>
<b>2</b>	<b>Quantum-corrected near-horizon geometry</b>	<b>4</b>
<b>3</b>	<b>Exact integral representation and Mordell structure of the metric factor</b>	<b>7</b>
3.1	From the Schwarzian kernel to an exact Gaussian-coth integral . . . . .	8
3.2	Large- $\xi$ asymptotics from the coth integral . . . . .	10

3.3	Mordell identity and complementary $q$ -channels . . . . .	10
3.4	General conformal dimension: ladders, Fermi towers, and infrared structure .	14
3.5	Variance of the Schwarzian kernel and the status of the averaged-metric prescription . . . . .	15
<b>4</b>	<b>Rectangular Wilson loop and the quark-antiquark potential</b>	<b>19</b>
4.1	Parametric formulas and renormalization . . . . .	19
4.2	Short distances: Coulomb, analytic series, and nonperturbative corrections .	21
4.3	Long distances: algebraic screening . . . . .	22
4.4	Detailed derivation of the IR scaling . . . . .	24
4.5	Numerical check of the connected branch in a smooth matched ansatz . . . .	26
4.6	Crossover scales and modular structure . . . . .	30
4.7	Limits of finite-order truncation . . . . .	31
<b>5</b>	<b>Outlook</b>	<b>34</b>
<b>A</b>	<b>Numerical implementation details</b>	<b>35</b>
A.1	Evaluation of $h(\xi)$ and $\mathcal{G}_0(\xi)$ . . . . .	35
A.2	Evaluation of the Wilson-loop parametric integrals . . . . .	36

# 1 Introduction

In the AdS/CFT correspondence [1, 2], the heavy quark-antiquark potential at strong coupling is computed from the area of a string worldsheet ending on a Wilson loop at the AdS boundary [3, 4]. In conformal backgrounds the result is purely Coulombic [3, 4]. Turning on a finite charge density changes this picture: near-extremal Reissner–Nordström (RN) AdS black branes [6] develop a near-horizon AdS<sub>2</sub> factor. On the field-theory side this AdS<sub>2</sub> × ℝ<sup>3</sup> region realizes a semi-local quantum liquid, or local quantum critical IR sector, with time scaling but no spatial scaling ( $z \rightarrow \infty$ ) [7, 8]. The planar spatial directions are compactified on  $T^3$  for the dimensional reduction below. The low-energy quantum fluctuations in this region are controlled by Jackiw–Teitelboim (JT) gravity and its Schwarzian boundary mode [7, 9–16] (see [17] for a review). The Schwarzian effective action governs the pattern of conformal symmetry breaking in nearly AdS<sub>2</sub> spacetimes [12, 14, 18], and its path integral can be evaluated exactly [15, 16, 19–21].

This framework has led to a broad program of re-examining classical holographic results with the inclusion of quantum corrections from the Schwarzian sector. Quantum averaging over the Schwarzian mode [22, 23] produces nontrivial radial kernels in the AdS<sub>2</sub> throat. The same Schwarzian kernel, or closely related near-AdS<sub>2</sub> quantum factors, enters a range of holographic observables, including Wilson loops [24], transport coefficients [25], hydrodynamic modes [26], the shear viscosity to entropy density ratio [27, 28], Hawking radiation spectra [29], and quasi-normal mode frequencies [30]. A common feature of these applications is that near-boundary or low-temperature expansions are often used beyond their manifest domain of validity, leading in some cases to qualitative modifications: a linear quark-antiquark potential [24], regularization of the fluid/gravity correspondence [26], and nontrivial low-temperature corrections to  $\eta/s$ , with regime-dependent conclusions about the Kovtun–Son–Starinets bound [27, 28, 31, 32].

Although the Schwarzian two-point function is exactly known [16, 19, 20], the induced radial profile  $h(\zeta)$ , with  $\zeta$  the AdS<sub>2</sub> radial coordinate (small near the boundary, large deep in the throat), has not previously been put in a form valid at all radial depths, as needed for analyzing holographic observables throughout the throat. In practical applications, the Schwarzian-corrected profile is represented by a near-boundary expansion in  $\zeta/C$ , truncated at finite order, where  $C$  is the Schwarzian coupling setting the scale that separates the classical and quantum regimes. This is reliable close to the AdS<sub>2</sub> boundary but not deep in the throat, where  $\zeta/C \gg 1$  and the asymptotic series loses uniform control. The issue is especially sharp for extended probes, whose saddles can penetrate to radial depths  $\zeta \gtrsim C$ . Wilson loops provide a useful diagnostic: one such finite-order implementation produced an approximately linear quark-antiquark potential at intermediate distances [24], reminiscent of the Cornell potential [33–35] and raising the question of holographic confinement [5, 36, 37]. Whether this linear behavior persists in the exact geometry is a nonperturbative question that cannot be settled without the full radial profile.

In this paper we obtain the exact Schwarzian-corrected metric factor  $h(\zeta)$  throughout the AdS<sub>2</sub> throat. The Schwarzian kernel reduces, after a change of variables, to a Gaussian-weighted integral against  $\coth(\pi y)$ . This exact integral has two uses:

1. Endpoint analysis directly yields the large- $\zeta$  behavior  $h(\zeta) \sim (\zeta/C)^{1/2}$ , rather than the polynomial growth implied by any finite truncation. A turning-point analysis in the near-horizon geometry then gives

$$E(L) \sim -\frac{\kappa_{\text{IR}}}{L^2}, \quad L \gg C, \quad (1)$$

for the renormalized quark-antiquark potential at large separation, with the coefficient  $\kappa_{\text{IR}}$  obtained in closed form (Eq. (108)). The potential exhibits *algebraic screening* — power-law decay rather than the exponential (Debye) screening of a finite-temperature plasma or the linear confinement of the truncated series. This power law is the Wilson-loop manifestation of the scale-free semi-local IR of the extremal brane. In Sec. 4.5 we also package the isolated throat result as a normalized universal curve, Eq. (101), so that the IR answer can be reused independently of the UV completion.

2. The integral is of the type classified by Mordell [38], and the Mordell identity provides an explicit closed-form evaluation of  $h(\zeta)$  (Eq. (43)) in terms of Appell–Lerch sums and theta functions [39, 40] — the  $q$ -series defined in Sec. 3.3 — with two complementary  $q$ -expansions, one suited to the near-boundary regime and one to the deep interior. Carrying out the required third derivative additionally generates the weight-2 Eisenstein series  $E_2$  [40], which mixes the two channels and is not itself part of the classical Mordell identity.

The strict linear confinement and putative mass gap found in finite-order analyses are not properties of the Schwarzian throat itself but of its truncation: the ratio  $\mathcal{G}_0(\zeta) := h(\zeta)/\zeta^2$ , which controls the effective string tension in the throat, decays monotonically rather than developing a minimum, and the tension vanishes deep in the throat.

The integral representation (15) directly yields the UV coefficients and complete monotonicity, and, by endpoint analysis, the IR  $(\zeta/C)^{1/2}$  asymptotics. The Mordell/Appell–Lerch evaluation (Sec. 3.3) goes further: by carrying out the required third parametric derivative of

the Mordell identity and exploiting a cancellation between the direct and  $S$ -dual Appell–Lerch channels at the degenerate point, we obtain the closed-form  $q/q^*$ -series (43). Any finite Taylor truncation misses the entire  $S$ -dual sector, controlled by  $e^{-\pi^2 C/\zeta}$ ; the Mordell formula makes these nonperturbative corrections quantitatively accessible.<sup>1</sup> The finite-order Wilson-loop analysis of [24] is recovered as the near-boundary approximation to the exact result.

Our exact representation of  $h(\zeta)$  holds at all radial depths of the  $\text{AdS}_2$  throat. By itself it does not determine the UV gluing to the asymptotically  $\text{AdS}_5$  region, which is theory-dependent: the same Schwarzian zero mode dominates universally at  $T \rightarrow 0$ , but the way this description emerges from the UV completion differs between, e.g., RN- $\text{AdS}_5$ , RN without cosmological constant, and near-extremal Kerr. Accordingly, the large- $L$  screening result depends only on the throat asymptotics and is robust, but intermediate-distance observables continue to depend on the matching prescription, which we take from [24]. We also include a numerical check (Sec. 4.5) in a simple matched geometry. This check is not a first-principles construction of the full quantum-corrected interpolation, but it verifies that the exact-throat screened saddle lies on a monotone, concave branch in the natural RN- $\text{AdS}_5$  completion and is not pre-empted by an intermediate cusp or maximal-separation transition. All results are at strict extremality ( $T = 0$ ). The zero-temperature kernel is the  $\beta \rightarrow \infty$  limit of the finite-temperature Schwarzian kernel (Sec. 3), and finite-temperature extensions are discussed in Sec. 5. The distinction is physical rather than technical: the infinitely long extremal throat supports the algebraic tail, while any nonzero temperature caps the throat and is expected to restore Debye-type exponential screening at sufficiently large separation.

The paper is organized as follows. Section 2 reviews the quantum-corrected geometry. Section 3 derives the exact integral representation, its large- $\zeta$  asymptotics, the closed-form Mordell/Appell–Lerch evaluation of  $h$ , the general- $\Delta$  kernel family, and the variance analysis of the averaged-metric prescription. Section 4 contains the main Wilson-loop analysis: the large-distance screening, the role of truncation, the turning-point derivations, and the observable-level exact-versus-truncated force comparison. Section 5 discusses open problems, and Appendix A records the numerical implementation details needed to reproduce the figures.

## 2 Quantum-corrected near-horizon geometry

*Conventions.* Throughout we use the dimensionless ratio  $\xi := \zeta/C$  and the purely imaginary modular parameter  $\tau := i\xi/\pi$  (so  $\Im\tau > 0$ ). The nome (the standard exponential parameter of elliptic function theory) is  $q := e^{\pi i\tau} = e^{-\xi}$ , and the image under the modular inversion  $\tau \mapsto -1/\tau$  gives  $q^* := e^{-\pi i/\tau} = e^{-\pi^2/\xi}$ . We follow the Jacobi  $\theta_{11}$  conventions of [40]. All Schwarzian/JT computations (Sec. 3) are carried out in Euclidean signature via the Wick rotation  $t \rightarrow -it_E$ . The Wilson-loop analysis (Sec. 4) is likewise performed in Euclidean signature; the static quark-antiquark potential is then extracted from the large- $T$  behavior of the Euclidean Wilson loop in the standard way [3].

---

<sup>1</sup>Here and below, “nonperturbative” refers to contributions of order  $\exp(-\pi^2 C/\zeta)$  that are invisible to any finite asymptotic expansion in  $\zeta/C$  of the zero-temperature Schwarzian kernel. This should not be confused with a nonperturbative completion of JT gravity in the matrix-integral or topology-summed sense [16].

We follow the RN-AdS<sub>5</sub> near-horizon setup and matching conventions of [24], while deriving below the exact form of the Schwarzian factor, valid at all radial depths. Consider a near-extremal Reissner–Nordström AdS<sub>5</sub> black brane with metric

$$ds^2 = -\frac{u^2}{L_{\text{AdS}}^2} f(u) dt^2 + \frac{L_{\text{AdS}}^2}{u^2} \frac{du^2}{f(u)} + \frac{u^2}{L_{\text{AdS}}^2} d\vec{x}^2, \quad (2)$$

where  $d\vec{x}^2$  is the flat metric on  $T^3$  and

$$f(u) = 1 - (1 + Q^2) \frac{u_T^4}{u^4} + Q^2 \frac{u_T^6}{u^6}. \quad (3)$$

The extremal limit corresponds to  $Q^2 \rightarrow 2$  at fixed horizon radius  $u_T$ . In this limit the near-horizon region develops an AdS<sub>2</sub> factor [7, 11, 14]. Introducing the small parameter  $\lambda \equiv (u - u_T)/u_T$  and zooming into the region  $\lambda \ll 1$ , one finds that the metric reduces to AdS<sub>2</sub>  $\times$   $T^3$  up to subleading terms. A convenient radial coordinate for the AdS<sub>2</sub> factor is

$$u = u_T + \frac{L_{\text{AdS}}^2}{12\zeta}, \quad (4)$$

in terms of which the near-horizon metric takes the form

$$ds_{\text{NHR}}^2 \approx \frac{L_2^2}{\zeta^2} (-dt^2 + d\zeta^2) + \frac{u_T^2}{L_{\text{AdS}}^2} d\vec{x}^2, \quad (5)$$

with an effective AdS<sub>2</sub> radius  $L_2$ .

Dimensional reduction on  $T^3$  and the near-horizon approximation lead to a JT gravity sector controlling quantum fluctuations of the AdS<sub>2</sub> factor [11, 14, 23]. The Euclidean JT path integral over Schwarzian modes produces an exact boundary two-point function [20]. Physically, the Schwarzian mode is the boundary graviton of the nearly AdS<sub>2</sub> geometry: it parametrizes reparametrizations of the AdS<sub>2</sub> boundary, and the JT path integral averages over all such reparametrizations. This averaging modifies the two-point kernel that controls the bulk geometry. In the averaged-metric prescription of [24], this modification is encoded in an effective quantum-corrected metric, written here in Euclidean signature (the Wick rotation  $t \rightarrow -it_E$  of the Lorentzian near-horizon form above, as appropriate for the Schwarzian path integral):

$$\langle ds_{\text{AdS}_2}^2 \rangle = h(\zeta) \frac{L_2^2}{\zeta^2} (dt^2 + d\zeta^2), \quad (6)$$

where the dimensionless metric factor  $h(\zeta)$  encodes all quantum corrections from the Schwarzian sector. Its normalization is fixed by requiring that  $h(\zeta) \rightarrow 1$  as  $\zeta \rightarrow 0$ , where the geometry approaches the AdS<sub>2</sub> boundary.

The exact expression for  $h(\zeta)$  follows from the Schwarzian boundary two-point function [14, 15, 19, 20, 41–43]. The parameter  $C$  introduced above plays the role of a JT heat capacity. In terms of it the quantum-averaged kernel is given by

$$G_{\partial\partial}(2\zeta) = \frac{1}{2C} \int_0^\infty d\omega \sinh(2\pi\sqrt{2C\omega}) e^{-2\zeta\omega} \Gamma(1 + i\sqrt{2C\omega})^2 \Gamma(1 - i\sqrt{2C\omega})^2. \quad (7)$$

Up to an overall normalization fixed by  $h(0) = 1$ , one can identify  $h(\zeta) \propto (\zeta/C)^2 G_{\partial\partial}(2\zeta)$ . Expanding this expression near the boundary gives

$$h(\zeta) \simeq 1 + c_2 \left(\frac{\zeta}{C}\right)^2 - c_3 \left(\frac{\zeta}{C}\right)^3 + c_4 \left(\frac{\zeta}{C}\right)^4 + \dots, \quad (8)$$

with the approximate coefficients  $c_2 = 3/(2\pi^4)$ ,  $c_3 = 15/(2\pi^6)$ ,  $c_4 = 315/(8\pi^8)$ . The exact coefficients, which differ by Riemann zeta factors, are derived in Sec. 3 once the exact integral representation is available.

In the far region the geometry is still described by the RN-AdS<sub>5</sub> metric (2), now dressed [24] by the same quantum factor  $h(u)$  that appears in the near-horizon AdS<sub>2</sub> patch. Following [24], we adopt a continuation/matching ansatz that extends the exact throat factor  $h(\zeta)$  into the far AdS<sub>5</sub> region, giving the quantum-corrected AdS<sub>5</sub> metric in the coordinates  $U \equiv u/\alpha'$ ,  $U_T \equiv u_T/\alpha'$  as

$$ds^2 = \alpha' \left[ \frac{U^2}{R^2} (f(U)h(U) dt^2 + d\vec{x}^2) + \frac{R^2}{U^2} f(U)^{-1} h(U) dU^2 \right], \quad (9)$$

where  $R$  is related to  $L_{\text{AdS}}$  and the effective string tension through  $\sqrt{\alpha'} = L_{\text{AdS}}/R$ . The function  $h(U)$  is the continuation of  $h(\zeta)$  from the AdS<sub>2</sub> region along the radial flow. Near the boundary the expansion (8) translates into an expansion of  $h(U)$  in inverse powers of  $(U - U_T)$ . From the point of view of Wilson loops, all observables depend on  $h(\zeta)$  only through the parametric integrals for the separation  $L$  and the Nambu–Goto action  $S_{\text{NG}}$ . The exact integral representation of  $h(\zeta)$  is directly applicable to the large- $L$  regime, where the worldsheet probes the AdS<sub>2</sub> throat. At intermediate and short distances, the Wilson loop observables depend on  $h(U)$  in the far region where the near-horizon and far metrics are matched; in that regime the results rely on the matching ansatz of [24]. The geometry and the string configurations are illustrated schematically in Fig. 1.

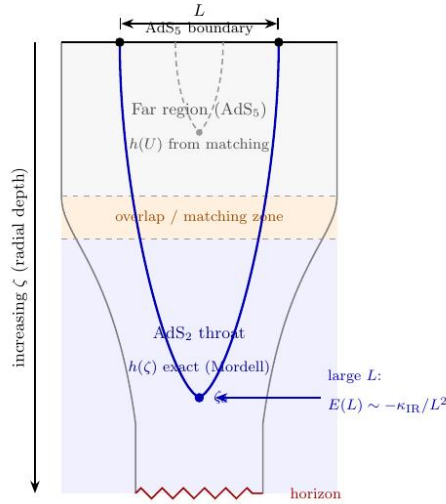


**Figure 1:** Schematic of the radial geometry and string worldsheets. The  $\text{AdS}_5$  boundary is at the top; radial depth  $\zeta$  increases downward toward the horizon. The near-horizon  $\text{AdS}_2$  throat (blue shading) is where the quantum metric factor  $h(\zeta)$  is controlled by the exact integral representation. The far region (gray) is the asymptotically  $\text{AdS}_5$  part, where  $h(U)$  is determined by matching. For large quark-antiquark separation  $L$  (solid curve), the string turning point  $\zeta_0$  lies deep in the throat, and the potential is governed by the exact  $h(\zeta) \sim \sqrt{\zeta}$  scaling. For small  $L$  (dashed curve), the turning point remains in the far region, and the results depend on the matched metric.

### 3 Exact integral representation and Mordell structure of the metric factor

In this section we reduce the Schwarzian kernel (7) to a one-dimensional integral of the type classified by Mordell [38]. Throughout this section we work in the dimensionless radial variable  $\xi := \zeta/C$  introduced above, writing  $h(\xi)$  for the same metric factor as  $h(\zeta)$ . Such integrals have appeared previously in the exact solution of Chern–Simons matrix models [44] and in related JT gravity contexts [42, 45]. An important distinction is worth noting at the outset: in the Chern–Simons setting of [44], the nome  $q$  is a root of unity ( $|q| = 1$ ) and the Mordell integral evaluates to finite sums involving Gauss-type exponential sums, whereas in the present JT gravity application  $q = e^{-\zeta/C}$  is real and lies strictly inside the unit disk. The Mordell identity then produces convergent  $q$ -series rather than finite sums, and the modular properties take a qualitatively different form. We extract the exact Gaussian-coth integral, its large- $\xi$  asymptotics, and, by carrying out the  $\partial_x^3$  differentiation of the Mordell identity, the explicit closed-form evaluation of  $h(\xi)$  in terms of Appell–Lerch sums, the Jacobi theta function, and the weight-2 Eisenstein series  $E_2$ . We then record the general-conformal-dimension extension and use it to quantify the variance of the averaged-metric prescription.

### 3.1 From the Schwarzian kernel to an exact Gaussian-coth integral

The four gamma functions in (7) can be grouped into two conjugate pairs. Using

$$\Gamma(1 + iy) \Gamma(1 - iy) = \frac{\pi y}{\sinh(\pi y)}, \quad (10)$$

the product of the four gamma functions becomes  $[\pi y / \sinh(\pi y)]^2$ , while the  $\sinh(2\pi y)$  factor from (7) combines with this to give

$$\sinh(2\pi y) \times \left[ \frac{\pi y}{\sinh(\pi y)} \right]^2 = 2\pi^2 y^2 \coth(\pi y). \quad (11)$$

Substituting  $y = \sqrt{2C\omega}$  (so  $d\omega = y dy/C$  and  $\omega = y^2/(2C)$ ) into (7), the factor  $2\pi^2 y^2$  together with  $d\omega = y dy/C$  and the prefactor  $1/(2C)$  yields

$$G_{\partial\partial}(2\zeta) = \frac{\pi^2}{C^2} \int_0^\infty dy y^3 e^{-(\zeta/C)y^2} \coth(\pi y). \quad (12)$$

The quantum metric factor is identified with the finite boundary limit of  $(\zeta/C)^2 C^2 G_{\partial\partial}(2\zeta)/\pi^2$ ; the explicit  $(\zeta/C)^2$  prefactor is required because  $G_{\partial\partial}$  diverges as  $\zeta^{-2}$  near the boundary, while  $h(\zeta) \rightarrow 1$ . Thus

$$h(\zeta) = N_h \left( \frac{\zeta}{C} \right)^2 \int_0^\infty dy y^3 e^{-(\zeta/C)y^2} \coth(\pi y), \quad (13)$$

where  $N_h$  is now fixed entirely by the boundary condition  $h(0) = 1$ . To determine  $N_h$ , write  $\coth(\pi y) = 1 + 2/(e^{2\pi y} - 1)$ , so

$$\lim_{\xi \rightarrow 0} \xi^2 \int_0^\infty dy y^3 e^{-\xi y^2} \coth(\pi y) = \int_0^\infty dy y^3 e^{-\xi y^2} \Big|_{\text{leading}} = \frac{\Gamma(2)}{2\xi^2} \xrightarrow{\xi^2 \times} \frac{1}{2}, \quad (14)$$

and  $h(0) = 1$  requires  $N_h = 2$ . The exact metric factor is therefore

$$h(\xi) = 2\xi^2 \int_0^\infty dy y^3 e^{-\xi y^2} \coth(\pi y). \quad (15)$$

*Near-boundary asymptotic expansion and exact coefficients.* The exact near-boundary expansion of (15), in the sense of an asymptotic expansion as  $\xi \rightarrow 0^+$ , is

$$h(\xi) \sim 1 + 4 \sum_{m=0}^{\infty} (-1)^m \frac{\Gamma(2m+4) \zeta_{\mathbb{R}}(2m+4)}{m! (2\pi)^{2m+4}} \xi^{m+2} = 1 + \frac{\xi^2}{60} - \frac{\xi^3}{126} + \frac{\xi^4}{240} - \frac{\xi^5}{396} + \dots, \quad (16)$$

where  $\zeta_{\mathbb{R}}$  denotes the Riemann zeta function. The coefficients are exact, but the series should not be interpreted as a convergent Taylor series at  $\xi = 0$ . The exact and approximate [24] coefficients are related by

$$c_k^{\text{exact}} = \zeta_{\mathbb{R}}(2k) c_k^{\text{approx}}, \quad k = 2, 3, 4, \dots, \quad (17)$$

where  $c_k$  denotes the coefficient of  $\xi^k$ . Equivalently, in the summation index of (16),  $c_{m+2}^{\text{exact}} = \zeta_{\mathbb{R}}(2m+4) c_{m+2}^{\text{approx}}$ . For low orders the  $\zeta_{\mathbb{R}}$  factors are numerically close to one, so the discrepancy

is mild; the approximate coefficients of [24] correspond to omitting the  $\zeta_{\text{R}}(2k)$  factor in each term. The approximate coefficients were used in [24] to compute Wilson loops to leading order in  $1/C$ .

The factorial growth of the coefficients makes the expansion asymptotic. For fixed truncation order  $N$  one may write

$$h(\xi) = 1 + 4\xi^2 \sum_{m=0}^N \frac{(-\xi)^m \Gamma(2m+4) \zeta_{\text{R}}(2m+4)}{m! (2\pi)^{2m+4}} + R_N(\xi), \quad (18)$$

with the simple bound

$$|R_N(\xi)| \leq 4\xi^{N+3} \frac{\Gamma(2N+6) \zeta_{\text{R}}(2N+6)}{(N+1)! (2\pi)^{2N+6}}, \quad \xi > 0. \quad (19)$$

The least term occurs at order  $m_{\text{opt}} \sim \pi^2/\xi$  [46], and the associated nonperturbative scale is  $e^{-\pi^2/\xi}$ . This is precisely the  $S$ -transformed scale  $q^* = e^{-\pi^2/\xi}$  appearing in the Mordell description (Sec. 3.3). Equivalently, if  $c_{m+2}$  denotes the coefficient of  $\xi^{m+2}$  in (16), then

$$c_{m+2} = (-1)^m \frac{2(m+1)\Gamma(m+5/2)}{\sqrt{\pi} \pi^{2m+4}} \zeta_{\text{R}}(2m+4) \sim (-1)^m \frac{2}{\sqrt{\pi} \pi^4} m^{5/2} m! \pi^{-2m}. \quad (20)$$

Thus the Borel transform of the UV series has radius  $\pi^2$ . Using  $\zeta_{\text{R}}(2m+4) = \sum_{k \geq 1} k^{-2m-4}$ , the natural singularity family is

$$t = -\pi^2 k^2, \quad k = 1, 2, \dots, \quad (21)$$

matching the poles of  $\coth(\pi y)$  at  $y = ik$ . The singularities lie on the negative Borel axis, so the UV expansion is directionally Borel summable for positive real  $\xi$ . The  $q^*$  channel should therefore be understood not as a positive-axis ambiguity, but as the modular/resurgent completion data controlling optimal truncation and analytic continuation across the negative Borel direction. Finite near-boundary truncations encode only this asymptotic UV sector and cannot be extrapolated reliably into the deep throat; the consequences for the Wilson-loop potential are discussed in Sec. 4.7.

*Range of validity of the near-boundary series.* Before using the truncated expansion (8) inside Wilson-loop integrals, we quantify where it is reliable. We compare  $h(\xi)$  from (15), evaluated by direct numerical quadrature, to its truncation through  $\mathcal{O}(\xi^4)$ . Figure 2 shows the near-boundary agreement and the corresponding relative error, making precise the domain in which the Taylor expansion can be used for short-distance observables and indicating when the exact integral is required.

Because  $y^3 \coth(\pi y)$  is even, one may symmetrize the integral and rewrite it as

$$\int_0^\infty dy y^3 e^{-ay^2} \coth(\pi y) = \int_{-\infty}^\infty dt \frac{t^3 e^{-at^2}}{e^{2\pi t} - 1}, \quad a = \frac{\zeta}{C} = \xi. \quad (22)$$

The right-hand side is a Gaussian-weighted moment against the kernel  $1/(e^{2\pi t} - 1)$ , and integrals of this type fall within the class studied by Mordell [38]. The connection to Mordell's formalism and its modular properties is made precise in Sec. 3.3.

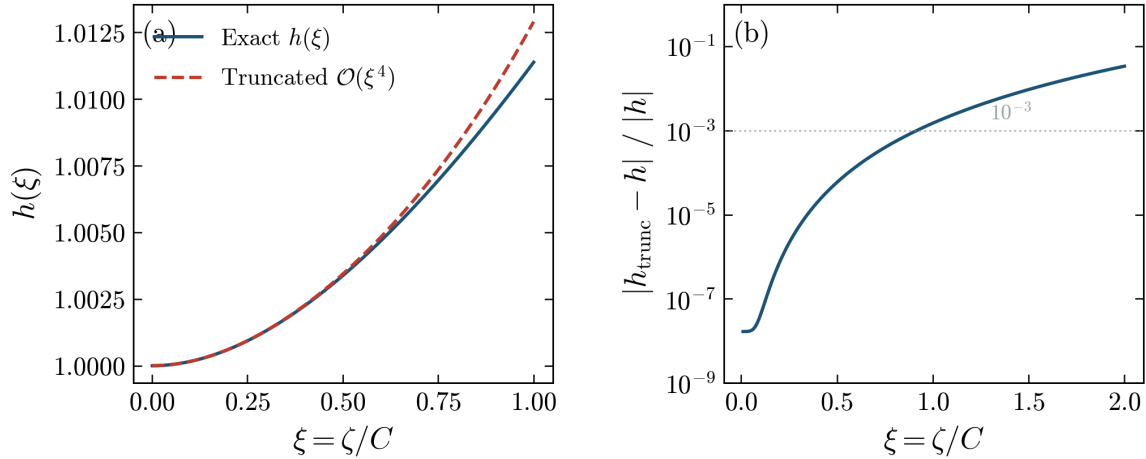


**Figure 2:** Near-boundary accuracy of the truncated expansion. (a) Exact quantum metric factor  $h(\xi)$  (solid) vs. the  $\mathcal{O}(\xi^4)$  truncation (dashed), with  $\xi \equiv \zeta/C$ . The two curves are indistinguishable for  $\xi \lesssim 0.5$ . (b) Relative error on a logarithmic scale. The error remains below  $10^{-3}$  for  $\xi \lesssim 0.9$  and grows rapidly beyond, motivating the exact integral representation for all infrared quantities.

### 3.2 Large- $\xi$ asymptotics from the coth integral

Before turning to the full Mordell evaluation, we extract the large- $\xi$  behavior of  $h(\xi)$  directly from (15). For  $\xi \gg 1$  the Gaussian factor  $e^{-\xi y^2}$  localizes the integral near  $y = 0$ , where  $\coth(\pi y) \simeq 1/(\pi y)$ . The dominant contribution is therefore

$$\int_0^\infty dy y^3 e^{-\xi y^2} \coth(\pi y) \simeq \frac{1}{\pi} \int_0^\infty dy y^2 e^{-\xi y^2} = \frac{\sqrt{\pi}}{4\pi \xi^{3/2}}, \quad \xi \rightarrow \infty. \quad (23)$$

Multiplying by  $2\xi^2$  gives the leading behavior; including the next terms in the Laurent expansion  $\coth(\pi y) = (\pi y)^{-1} + \pi y/3 - \pi^3 y^3/45 + \dots$  and integrating term by term yields

$$h(\xi) \sim \frac{1}{2\sqrt{\pi}} \xi^{1/2} + \frac{\pi^{3/2}}{4} \xi^{-1/2} - \frac{\pi^{7/2}}{24} \xi^{-3/2} + \dots, \quad \xi \rightarrow \infty. \quad (24)$$

The leading  $\sqrt{\xi}$  coefficient  $1/(2\sqrt{\pi}) \approx 0.2821$  is the input for the long-distance Wilson loop analysis. The subleading powers of  $1/\xi$  form a divergent asymptotic series. In addition, the Mordell identity discussed below implies the existence of exponentially suppressed corrections of order  $e^{-\xi}$  from the  $q$ -expansion, which are invisible to the asymptotic power series. Figure 3 compares the exact profile of  $h(\xi)$  with the truncated series and the IR asymptotics (24) across the full range of depths.

### 3.3 Mordell identity and complementary $q$ -channels

Introduce the Mordell integral [38] (in the normalization used in modern treatments)

$$\mathcal{M}(x, \theta; \tau) := \int_{-\infty}^{\infty} \frac{e^{\pi i \tau t^2 - 2\pi x t}}{e^{2\pi t} - e^{2\pi i \theta}} dt, \quad \Im \tau > 0. \quad (25)$$

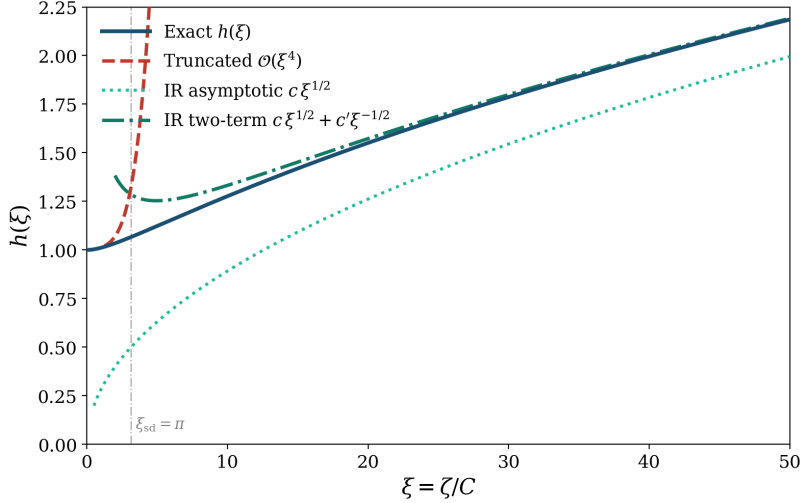


**Figure 3:** Global profile of the quantum metric factor  $h(\xi)$  as a function of  $\xi \equiv \zeta/C$  (solid), compared with the  $\mathcal{O}(\xi^4)$  truncated series (dashed) and two IR asymptotic approximations from Eq. (24): the leading term  $c\xi^{1/2}$  with  $c = 1/(2\sqrt{\pi})$  (dotted), and the two-term approximation  $c\xi^{1/2} + c'\xi^{-1/2}$  with  $c' = \pi^{3/2}/4$  (dash-dotted). The truncation diverges for  $\xi \gtrsim 2$ . The leading  $\sqrt{\xi}$  term undershoots by  $\sim 9\%$  at  $\xi = 50$ ; including the subleading  $\xi^{-1/2}$  correction reduces the error to  $\sim 0.3\%$ , confirming that the two-term asymptotic provides an accurate description of  $h$  deep in the throat. The vertical dash-dotted line marks the self-dual point  $\xi_{\text{sd}} = \pi$  where the two modular expansion parameters  $|q| = e^{-\xi}$  and  $|q^*| = e^{-\pi^2/\xi}$  are equal.

Here  $x$  is an auxiliary parameter in the sense of Mordell [38] that generates polynomial moments of  $t$  by differentiation; it is unrelated to the boundary spatial coordinate  $x$  used later in the worldsheet embedding.

In our application we only need parametric derivatives of (25). Indeed, differentiating under the integral sign shows that moments of  $t$  are generated by  $x$ -derivatives:

$$\int_{-\infty}^{\infty} dt \frac{t^3 e^{\pi i \tau t^2}}{e^{2\pi t} - e^{2\pi i \theta}} = -\frac{1}{8\pi^3} \partial_x^3 \mathcal{M}(x, \theta; \tau) \Big|_{x=0}. \quad (26)$$

For  $\theta = 0$  the denominator in (25) vanishes at  $t = 0$ , so the raw integral  $\mathcal{M}(x, 0; \tau)$  is naturally understood by analytic continuation in  $\theta$  (or, equivalently, a principal-value contour prescription). In the present application the relevant object is  $\partial_x^3 \mathcal{M}$  evaluated at  $x = 0$ : the three  $x$ -derivatives bring down a factor of  $t^3$ , and the would-be  $1/t$  singularity at the origin becomes integrable. Consequently the moment integral in (26) is absolutely convergent and the  $\theta \rightarrow 0$  limit can be taken without ambiguity. More precisely, the Mordell identity (30) holds for generic  $\theta$ , and after the  $\partial_x^3$  differentiation the resulting integrands are uniformly bounded by a  $\theta$ -independent  $L^1$  function (provided by the Gaussian decay  $e^{-\xi t^2}$ ), so the identity extends to  $\theta \rightarrow 0$  by dominated convergence.

Combining (15) and (22) with (26) gives the relation between  $h(\zeta)$  and the Mordell integral:

$$h(\zeta) = -\frac{1}{4\pi^3} \left(\frac{\zeta}{C}\right)^2 \partial_x^3 \mathcal{M}(x, \theta; \tau) \Big|_{x=0, \theta \rightarrow 0, \tau = i\zeta/(\pi C)}. \quad (27)$$

Mordell [38] showed that (25) can be evaluated in closed form. Following the conventions of [40], in the notation  $q = e^{\pi i \tau}$  and  $\Im \tau > 0$ , define

$$i F(z, \tau) := \sum_{m=-\infty}^{\infty} \frac{(-1)^m q^{m^2+m+1/4} e^{(2m+1)\pi i z}}{1 + q^{2m+1}}, \quad (28)$$

$$i \theta_{11}(z, \tau) := \sum_{m=-\infty}^{\infty} (-1)^m q^{m^2+m+1/4} e^{(2m+1)\pi i z}. \quad (29)$$

Here  $\theta_{11}$  is the standard odd Jacobi theta function [40] and  $F$  is an Appell–Lerch sum [39] (the ratio  $F/\theta_{11}$  is the holomorphic Appell–Lerch, or mock-Jacobi, object whose completed form has the modular behavior described by Zwegers [39]). In terms of these functions, Mordell’s identity reads [38]

$$\mathcal{M}(x, \theta; \tau) = e^{-\pi i(\theta^2 \tau + 2\theta x + 2\theta)} \frac{F\left(\frac{x+\theta\tau}{\tau}, -\frac{1}{\tau}\right) + i\tau F(x + \theta\tau, \tau)}{\tau \theta_{11}(x + \theta\tau, \tau)}. \quad (30)$$

The identity (30) provides two complementary expansions: the term  $F(x + \theta\tau, \tau)$  is a series in  $q = e^{-\zeta/C}$  suited to large  $\zeta$ , while  $F((x + \theta\tau)/\tau, -1/\tau)$  is an  $S$ -transformed series in  $q^* = e^{-\pi^2 C/\zeta}$  suited to small  $\zeta$ . We now carry out the  $\partial_x^3$  differentiation and extract the explicit dual  $q$ -series for  $h(\xi)$ .

*Holomorphicity at the degenerate point.* Set  $z = x + \theta\tau$ , write  $\tau_* := -1/\tau$  for the modular-inverted parameter, and define

$$\Phi(z; \tau) := F\left(\frac{z}{\tau}, \tau_*\right) + i\tau F(z, \tau), \quad R(z; \tau) := \frac{\Phi(z; \tau)}{\tau \theta_{11}(z, \tau)}. \quad (31)$$

The  $S$ -transformation identity for the Appell–Lerch sum implies that the numerator vanishes at the same point where  $\theta_{11}$  has its simple zero:

$$\Phi(0; \tau) = F(0, \tau_*) + i\tau F(0, \tau) = 0. \quad (32)$$

Since  $\theta_{11}(z, \tau)$  has a simple zero at  $z = 0$ , the cancellation (32) implies that  $R(z; \tau)$  is holomorphic at  $z = 0$ , despite the individual pole of  $\Phi/(\tau\theta_{11})$ .

*Extraction of  $\partial_x^3$ .* From the Mordell identity (30),

$$\mathcal{M}(x, \theta; \tau) = e^{-\pi i(\theta^2 \tau + 2\theta)} e^{-2\pi i \theta x} R(x + \theta\tau; \tau). \quad (33)$$

Since  $R$  is holomorphic at the origin, the exponential prefactor  $e^{-2\pi i \theta x}$  contributes only subleading terms in  $\theta$ , and the  $\theta \rightarrow 0$  limit gives

$$\partial_x^3 \mathcal{M}(x, \theta; \tau) \Big|_{x=0, \theta \rightarrow 0} = R'''(0; \tau). \quad (34)$$

To compute  $R'''(0)$ , expand  $\Phi$  and  $\Theta \equiv \theta_{11}$  in Taylor series around  $z = 0$ . Write  $\phi_j := \tau^{-j} F^{(j)}(0, \tau_*) + i\tau F^{(j)}(0, \tau)$ , so that  $\Phi(z) = \phi_1 z + \frac{1}{2} \phi_2 z^2 + \frac{1}{6} \phi_3 z^3 + \frac{1}{24} \phi_4 z^4 + \dots$ . Expanding  $\Theta = \Theta_1 z + \frac{1}{6} \Theta_3 z^3 + \dots$  (only odd powers, since  $\theta_{11}$  is odd) and dividing, one obtains

$$R(z) = \frac{1}{\tau \Theta_1} \left[ \phi_1 + \frac{\phi_2}{2} z + \left( \frac{\phi_3}{6} - \frac{\phi_1 \Theta_3}{6 \Theta_1} \right) z^2 + \left( \frac{\phi_4}{24} - \frac{\phi_2 \Theta_3}{12 \Theta_1} \right) z^3 + O(z^4) \right], \quad (35)$$

whence

$$R'''(0; \tau) = \frac{1}{\tau \Theta_1} \left[ \frac{\phi_4}{4} - \frac{\phi_2 \Theta_3}{2\Theta_1} \right]. \quad (36)$$

*Explicit  $q/q^*$ -series formula.* Using the standard identity  $\theta_{11}'''(0, \tau)/\theta_{11}'(0, \tau) = -\pi^2 E_2(\tau)$  [40], where  $E_2(\tau) = 1 - 24 \sum_{n=1}^{\infty} \sigma_1(n) q^{2n}$  is the weight-2 Eisenstein series, Eqs. (34) and (36) give

$$h(\xi) = -\frac{\xi^2}{16\pi^3 \tau \theta_{11}'(0, \tau)} \left[ \phi_4 + 2\pi^2 E_2(\tau) \phi_2 \right]_{\tau=i\xi/\pi}, \quad (37)$$

with

$$\phi_2 = \tau^{-2} F''(0, \tau_*) + i\tau F''(0, \tau), \quad (38)$$

$$\phi_4 = \tau^{-4} F^{(4)}(0, \tau_*) + i\tau F^{(4)}(0, \tau). \quad (39)$$

**Remark 1.** *The final answer involves  $F''$  and  $F^{(4)}$ , not  $F'''$ . This is structural: the third  $x$ -derivative acts on a quotient whose denominator vanishes linearly, so the  $z^3$  coefficient of  $R$  requires the  $z^4$  coefficient of  $\Phi$ .*

*Explicit  $q/q^*$ -series form.* For  $\tau = i\xi/\pi$  we have  $q = e^{-\xi}$ ,  $q^* = e^{-\pi^2/\xi}$ , and  $s := \xi/\pi = -i\tau$ . Define

$$T(q) := 2 \sum_{m=0}^{\infty} (-1)^m (2m+1) q^{(m+1/2)^2}, \quad (40)$$

and, for  $r = 2, 4$ ,

$$L_r(q) := \sum_{m=0}^{\infty} (-1)^m (2m+1)^r q^{(m+1/2)^2} \frac{1 - q^{2m+1}}{1 + q^{2m+1}}. \quad (41)$$

Then  $\theta_{11}'(0, \tau) = \pi T(q)$ , and the Eisenstein series in the  $q$ -variable is

$$E_2(q) := 1 - 24 \sum_{n=1}^{\infty} \sigma_1(n) q^{2n}. \quad (42)$$

After reducing to real form,

$$h(\xi) = \frac{\pi^2 s}{16 T(q)} \left[ s^{-4} L_4(q^*) - s L_4(q) + 2E_2(q) (s^{-2} L_2(q^*) + s L_2(q)) \right]. \quad (43)$$

Equation (43) is our closed-form evaluation of  $h(\xi)$ , obtained by applying Mordell's identity to the exact integral (15). The  $q^*$ -terms ( $L_r(q^*)$ ) are the  $S$ -dual channel, exponentially small near the boundary ( $\xi \ll 1$ ). The  $q$ -terms ( $L_r(q)$ ) are exponentially small deep in the throat ( $\xi \gg 1$ ). The Eisenstein series  $E_2$  mixes the two channels, reflecting the quasi-modular (rather than strictly modular) nature of the weight-2 object. We emphasize that  $E_2$  is not present in Mordell's classical identity (30), which involves only the Appell–Lerch and theta functions. It is generated here by the third derivative  $\partial_x^3$ , which forces the third Taylor coefficient of the odd theta function  $\theta_{11}$  at the origin and hence the ratio  $\theta_{11}'''(0, \tau)/\theta_{11}'(0, \tau) = -\pi^2 E_2(\tau)$

[Eq. (37)]. The appearance of  $E_2$  in the closed form for  $h$  is thus a feature of the present construction, not of the underlying Mordell identity.

Direct summation of (43) reproduces the Gaussian-coth integral to the full working precision of the numerical evaluation ( $\approx 12$  significant figures). For instance, quoting twelve figures,  $h(0.5) = 1.00337597688$ ,  $h(3) = 1.06251163839$ , and  $h(10) = 1.27670420355$ .

Although the individual theta/Appell–Lerch sums  $L_r(q^*)$  and  $T(q)$  contain the standard  $q_*^{1/4}$ -type theta prefactor, the same factor appears in  $T(q)$  after modular transformation and cancels in the ratio; the nonperturbative scale of the near-boundary completion is therefore  $q^* = e^{-\pi^2/\xi}$ , in agreement with the optimal-truncation estimate of Sec. 3.1.

The quasi-modular term has a direct interpretation: it is the curvature of the  $\theta_{11}$  zero that cancels the Appell–Lerch pole. Thus the two channels are not independent  $q$ - and  $q^*$ -series; they are mixed by the weight-two modular connection  $E_2$ . This is the precise sense in which the exact throat geometry is a quasi-modular, rather than strictly modular, completion of the near-boundary expansion.

We note that the kernel  $G_{\partial\partial}$  used throughout this paper is the strict  $\beta \rightarrow \infty$  limit of the finite-temperature double-spectral representation of [16, 20]; thus the zero-temperature results form an exact subsector of the full thermal theory, and finite-temperature extensions correspond to controlled deformations of this limit rather than independent assumptions.

### 3.4 General conformal dimension: ladders, Fermi towers, and infrared structure

The same reduction applies to a Schwarzian bilocal of arbitrary conformal dimension. With the normalization chosen so that  $h_\Delta(0) = 1$ , define

$$h_\Delta(\xi) = \frac{\xi^{2\Delta}}{\pi^2 \Gamma(2\Delta)} \int_0^\infty dy y \sinh(2\pi y) |\Gamma(\Delta + iy)|^4 e^{-\xi y^2}, \quad \Delta > 0. \quad (44)$$

For  $\Delta = 1$ , the identity  $|\Gamma(1 + iy)|^2 = \pi y / \sinh(\pi y)$  reduces (44) to the Gaussian-coth integral (15). The recursion

$$|\Gamma(\Delta + 1 + iy)|^4 = (\Delta^2 + y^2)^2 |\Gamma(\Delta + iy)|^4 \quad (45)$$

turns each integer or half-integer tower into a finite differential ladder: multiplication by  $y^2$  inside the integral is  $-\partial_\xi$ , so the next rung is obtained from the preceding seed by the operator  $(\Delta^2 - \partial_\xi)^2$ , followed only by the elementary change of the normalizing factor  $\xi^{2\Delta}/\Gamma(2\Delta)$ . Consequently any closed  $q/q^*$  representation for a seed propagates through the tower by term-by-term differentiation.

For positive integers this gives the moment family

$$h_n(\xi) := \frac{\langle \mathcal{B}_1^n \rangle}{\langle \mathcal{B}_1 \rangle_{\text{cl}}^n} = \frac{2\xi^{2n}}{\Gamma(2n)} \int_0^\infty dy y^3 \left[ \prod_{j=1}^{n-1} (j^2 + y^2) \right]^2 e^{-\xi y^2} \coth(\pi y), \quad h_n(0) = 1. \quad (46)$$

For half-integers the seed is instead a Fermi-type kernel. Since  $|\Gamma(1/2 + iy)|^2 = \pi / \cosh(\pi y)$ ,

$$h_{1/2}(\xi) = 2\xi \int_0^\infty dy y \tanh(\pi y) e^{-\xi y^2}. \quad (47)$$

The near-boundary expansion follows by writing  $\tanh(\pi y) = 1 - 2/(e^{2\pi y} + 1)$ ; relative to the Bose integrals in (16), the even zeta values are replaced by the Dirichlet eta combination  $(1 - 2^{1-2k})\zeta_R(2k)$ . In particular

$$h_{1/2}(\xi) = 1 - \frac{\xi}{12} + \frac{7\xi^2}{480} - \frac{31\xi^3}{8064} + O(\xi^4), \quad \xi \rightarrow 0^+. \quad (48)$$

This is qualitatively different from the dimension-one kernel: the half-integer seed initially decreases rather than grows.

The infrared endpoint is universal and is governed only by the small- $y$  expansion of the spectral density. Expanding  $y \sinh(2\pi y) |\Gamma(\Delta + iy)|^4$  at fixed  $\Delta$  gives

$$h_\Delta(\xi) \simeq \frac{\Gamma(\Delta)^4}{\Gamma(2\Delta)} \frac{\xi^{2\Delta-3/2}}{2\sqrt{\pi}} \left[ 1 + \frac{\pi^2 - 3\psi'(\Delta)}{\xi} + O(\xi^{-2}) \right], \quad \xi \rightarrow \infty. \quad (49)$$

Here  $\psi'$  is the trigamma function. At  $\Delta = 1$ , where  $\psi'(1) = \pi^2/6$ , Eq. (49) reduces to (24). The nonperturbative scales also have a simple geography. The poles of  $|\Gamma(\Delta + iy)|^2$  at  $y = \pm i(\Delta + m)$  generate the deep-throat recessive scale

$$q_\Delta = e^{-\Delta^2 \xi}, \quad \xi_{sd}(\Delta) = \frac{\pi}{\Delta}, \quad (50)$$

where the second equation is the point at which  $q_\Delta$  has the same size as the UV modular scale  $q^* = e^{-\pi^2/\xi}$ . In the integer tower the polynomial zeros in (46) cancel the sub- $\Delta$  rungs of this pole sequence, so the first surviving exponential is precisely  $e^{-n^2 \xi}$ .

There is also a modular dichotomy. Integer  $\Delta$  sits at the degenerate characteristic used above: the cancellation  $\Phi(0; \tau) = 0$  exposes the quasi-modular connection term  $E_2$ . Half-integer  $\Delta$  instead sits at the regular characteristic  $\theta = 1/2$ ; the corresponding Mordell integral belongs to the family of mock theta functions classified by Zwegers [39] and transforms with a genuine weight-one-half  $S$ -factor before the differential ladder is applied. Thus the appearance of  $E_2$  is a property of the integer-dimension, degenerate-characteristic kernel, not an unavoidable feature of every Schwarzian radial factor.

### 3.5 Variance of the Schwarzian kernel and the status of the averaged-metric prescription

All Wilson-loop results in this paper, like those of [24], are computed in the *mean* geometry: the worldsheet functional is evaluated on the quantum-averaged metric (6)–(9), i.e. we compute  $W[\langle g \rangle]$ . The JT path integral itself defines instead  $\langle W[g] \rangle$ , the Schwarzian average of the worldsheet observable, and because the Nambu–Goto action is nonlinear in the metric the two differ. Schematically, at fixed embedding,

$$\log \langle W \rangle = -S_{\text{NG}}[\langle g \rangle] - \left( \langle S_{\text{NG}}[g] \rangle - S_{\text{NG}}[\langle g \rangle] \right) + \frac{1}{2} \text{Var} S_{\text{NG}}[g] + \dots, \quad (51)$$

where both correction terms are quadratic in metric fluctuations at leading order and are controlled by connected correlators of the Schwarzian bilocal at split arguments, which are exactly known [19, 20] (re-extremization of the embedding contributes at the same

order). Both corrections raise  $\log\langle W \rangle$ : the variance is nonnegative, and concavity of  $\sqrt{\det g}$  on positive metrics gives  $\langle S_{\text{NG}}[g] \rangle \leq S_{\text{NG}}[\langle g \rangle]$  at fixed embedding, so to this order metric fluctuations *deepen* the potential rather than stiffen it; the mean-geometry estimate, if anything, underestimates screening. The exposure to the difference is largest precisely where our main result lives, deep in the throat. In this subsection we quantify it: the variance of the very kernel that defines  $h$  is exactly computable within the same Gaussian-coth/Mordell toolbox, and it delimits where the mean geometry is a controlled proxy for the fluctuating one.

*Exact variance of the defining kernel.* The kernel (7) is the zero-temperature expectation value of the dimension-one Schwarzian bilocal

$$\mathcal{B}_\Delta(t_1, t_2) := \left[ \frac{f'(t_1) f'(t_2)}{(f(t_1) - f(t_2))^2} \right]^\Delta, \quad G_{\partial\partial}(2\zeta) \propto \langle \mathcal{B}_1(2\zeta) \rangle, \quad (52)$$

where  $f$  is the boundary reparametrization and  $\langle \cdot \rangle$  the Schwarzian path integral. Geometrically  $\mathcal{B}_1 = e^{-\ell_{\text{ren}}}$ , with  $\ell_{\text{ren}}$  the renormalized geodesic length between the two boundary points, so that  $h(\zeta) = \langle e^{-(\ell_{\text{ren}} - \ell_{\text{cl}})} \rangle$  is an *annealed* average over length fluctuations. Because  $\mathcal{B}_\Delta$  is a functional of  $f$  rather than an operator with nontrivial ordering, its square at coincident endpoints is literally the dimension-two bilocal,  $\mathcal{B}_1^2 = \mathcal{B}_2$ , and the variance of the defining kernel is the  $\Delta = 2$  member of the exactly solvable family [15, 19, 20]. Since  $|\Gamma(2+iy)|^2 = (1+y^2)|\Gamma(1+iy)|^2$ , the reduction of Sec. 3 applies verbatim with the polynomial  $y^3 \mapsto y^3(1+y^2)^2$ , and the normalized second moment is

$$h_2(\xi) := \frac{\langle \mathcal{B}_2(2\zeta) \rangle}{\mathcal{B}_2^{\text{cl}}(2\zeta)} = \frac{\xi^4}{3} \int_0^\infty dy (y^3 + 2y^5 + y^7) e^{-\xi y^2} \coth(\pi y), \quad h_2(0) = 1. \quad (53)$$

The  $y^5$  and  $y^7$  moments are the derivative moments  $(-1)^n \mathcal{G}_0^{(n)}(\xi) = 2 \int_0^\infty dy y^{3+2n} e^{-\xi y^2} \coth(\pi y)$  of the confinement indicator  $\mathcal{G}_0(\xi) := h(\xi)/\xi^2$  (cf. Theorem 3), so the relative variance has the closed form

$$\mathcal{V}(\xi) := \frac{\langle \mathcal{B}_1^2 \rangle - \langle \mathcal{B}_1 \rangle^2}{\langle \mathcal{B}_1 \rangle^2} = \frac{h_2(\xi)}{h(\xi)^2} - 1 = \frac{\mathcal{G}_0(\xi) - 2\mathcal{G}_0'(\xi) + \mathcal{G}_0''(\xi)}{6\mathcal{G}_0(\xi)^2} - 1, \quad (54)$$

an exact identity at all radial depths. Each moment is a higher  $x$ -derivative of the Mordell integral at the degenerate point [cf. (26)], so  $\mathcal{V}$  inherits a closed  $q/q^*$ -series representation of precisely the type (43), with  $\partial_x^5$  and  $\partial_x^7$  replacing  $\partial_x^3$ ; we do not display it.

*Asymptotics and crossover.* Near the boundary the polynomial Gaussian moments in (53) are exact and terminate,  $h_2(\xi) = 1 + \frac{2}{3}\xi + \frac{1}{6}\xi^2 + \mathcal{O}(\xi^4)$ , with corrections of order  $\xi^4$  from the Bose tail  $\coth(\pi y) - 1$ , in the same asymptotic sense as (16); combining with (16),

$$\mathcal{V}(\xi) = \frac{2}{3}\xi + \frac{2}{15}\xi^2 - \frac{2}{315}\xi^3 + \mathcal{O}(\xi^4), \quad \xi \rightarrow 0^+. \quad (55)$$

Relative fluctuations of the kernel grow *linearly* in  $\zeta/C$  — the expected one-loop behavior of the weakly coupled Schwarzian mode, here with exact coefficient 2/3. Deep in the throat, the endpoint analysis of Sec. 3.2 applied to numerator and denominator of (54) gives

$$\mathcal{V}(\xi) \simeq \frac{\sqrt{\pi}}{3} \xi^{3/2} - \sqrt{\pi} \left( \frac{\pi^2}{6} - 1 \right) \xi^{1/2} + \dots \simeq \frac{1}{6\mathcal{G}_0(\xi)}, \quad \xi \rightarrow \infty, \quad (56)$$

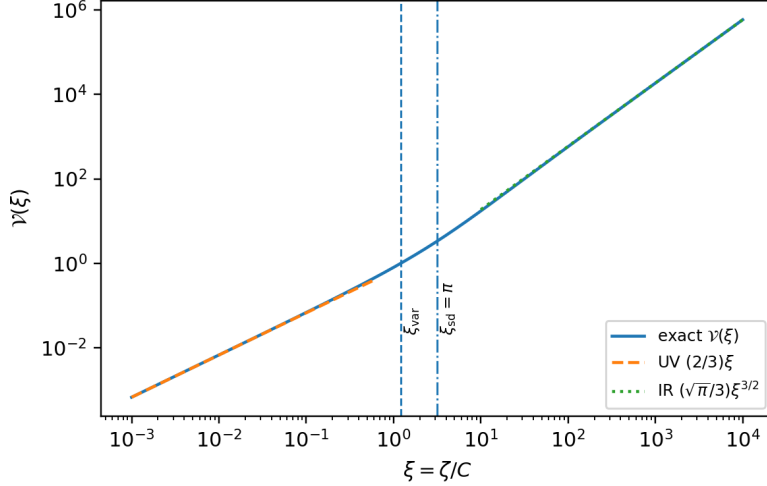


**Figure 4:** Relative variance  $\mathcal{V}(\xi)$  of the Schwarzian kernel. The UV line is the exact leading law  $\mathcal{V} \simeq (2/3)\xi$ , while the IR line is  $\mathcal{V} \simeq (\sqrt{\pi}/3)\xi^{3/2}$ . The vertical lines mark the point  $\xi_{\text{var}} \simeq 1.216$  where the variance equals the squared mean and the self-dual depth  $\xi_{\text{sd}} = \pi$ .

the last form holding because  $\mathcal{G}'_0$  and  $\mathcal{G}''_0$  are subleading at the spectral edge. Numerically (Fig. 4; same quadrature as Appendix A.1):  $\mathcal{V}(1) = 0.7957$ ;  $\mathcal{V} = 1$  at  $\xi_{\text{var}} \simeq 1.216$ ;  $\mathcal{V}(\pi) \simeq 3.31$  at the self-dual point;  $\mathcal{V}/\xi^{3/2} \rightarrow \sqrt{\pi}/3 = 0.5908$  (reaching 0.5907 by  $\xi = 10^4$ ), and the two-term form (56) is accurate to  $3 \times 10^{-5}$  relative at  $\xi = 10^3$ . Kernel fluctuations thus become comparable to the mean at  $\zeta \simeq 1.2C$  — essentially the scale at which the truncated series of [24] loses control — and dominate beyond. In particular, at  $\xi \simeq 4.19$ , where the truncation places its spurious confining minimum (Fig. 8), the relative variance is already  $\mathcal{V} \simeq 4.9$ : the putative confining wall sits in a region where the geometry is fluctuation-dominated, compounding the truncation artifact established in Theorem 3.

*All moments, spectral-edge universality, and non-self-averaging.* The integer moment formula (46) shows that every moment remains in the Gaussian-coth, hence Mordell, class. Deep in the throat all these moments are controlled by the same spectral edge summarized in (49): although  $h_n(\xi) \sim \xi^{2n-3/2}$  after classical normalization,  $\langle \mathcal{B}_1^n \rangle$  itself falls as  $c_n \zeta^{-3/2}$  for every  $n$ . Therefore all normalized moment ratios diverge,

$$\frac{\langle \mathcal{B}^n \rangle}{\langle \mathcal{B} \rangle^n} \sim \xi^{3(n-1)/2}, \quad \xi \rightarrow \infty. \quad (57)$$

The distribution of  $e^{-\ell_{\text{ren}}}$  deep in the throat is heavy-tailed: its mean is dominated by rare, anomalously short renormalized geodesics, while by Jensen’s inequality [47]  $\langle e^{-\ell} \rangle \geq e^{-\langle \ell \rangle}$  the typical throat is *longer* than the annealed geometry suggests. The kernel is not self-averaging for  $\zeta \gtrsim C$ , and (6) should be understood there as the mean of a broad distribution rather than the metric seen by a typical configuration.

*What is prescription-robust.* It is natural to ask which conclusions survive once the averaged-metric (annealed,  $\Delta = 1$ ) choice is relaxed within this family. Repeating the construction of Sec. 2 with a dimension- $\Delta$  bilocal — reading the Weyl factor from  $\zeta^{2\Delta} \langle \mathcal{B}_\Delta(2\zeta) \rangle$  through

the same geodesic dictionary, under which a classical dimension- $\Delta$  two-point function on the dressed metric scales as  $h(\zeta)^\Delta/(\Delta t)^{2\Delta}$  — assigns the metric factor  $h_\Delta(\xi)^{1/\Delta}$ . The answer then separates cleanly.

**Proposition 2** (Moment-robust absence of a confining minimum). *For every  $\Delta > 0$  let  $h_\Delta(\xi) := \langle \mathcal{B}_\Delta(2\zeta) \rangle / \mathcal{B}_\Delta^{\text{cl}}(2\zeta)$  denote the normalized  $\Delta$ -moment of the bilocal, and let  $h_\Delta^{1/\Delta}$  be the metric factor a dimension- $\Delta$  probe assigns. Then*

$$\mathcal{G}_0^{(\Delta)}(\xi) := \frac{h_\Delta(\xi)^{1/\Delta}}{\xi^2} \quad (58)$$

is strictly decreasing on  $(0, \infty)$ . In particular, no moment-based effective geometry in this family develops a finite-depth minimum of the effective string tension.

*Proof.*  $h_\Delta(\xi)^{1/\Delta}/\xi^2 = c_\Delta \langle \mathcal{B}_\Delta(2\zeta) \rangle^{1/\Delta}$  with  $c_\Delta > 0$ , and  $\langle \mathcal{B}_\Delta(2\zeta) \rangle = \int_0^\infty d\omega \rho_\Delta(\omega) e^{-2\zeta\omega}$  with  $\rho_\Delta(\omega) \propto \sinh(2\pi\sqrt{2C\omega}) |\Gamma(\Delta + i\sqrt{2C\omega})|^4 \geq 0$  [the  $\Delta$ -generalization of (7)] is the Laplace transform of a nonzero positive measure, hence strictly decreasing in  $\zeta$ ; composition with the increasing map  $x \mapsto x^{1/\Delta}$  preserves strict decrease.  $\square$

The conclusion that the confining minimum of the truncated series is an artifact is therefore independent of which moment of the fluctuating geometry one declares to be “the” metric. The infrared *exponent*, by contrast, is not: from (49),

$$h_\Delta(\xi)^{1/\Delta} \sim \xi^{a(\Delta)}, \quad a(\Delta) = 2 - \frac{3}{2\Delta}, \quad (59)$$

so the screening law depends on the probe dimension through the general-exponent analysis of Sec. 4.4 [cf. (96)]:  $\Delta = 1$ , the kernel of [24] and of this paper, gives  $a = \frac{1}{2}$  and  $E \sim -\kappa_{\text{IR}}/L^2$ , while already at  $\Delta = 2$  one finds  $a = \frac{5}{4} > 1$ , for which the renormalized energy integral over the throat (Sec. 4.4) no longer converges and the structure of the IR analysis changes qualitatively. By Lyapunov’s moment inequality [47],  $h_\Delta^{1/\Delta}$  is nondecreasing in  $\Delta$  at fixed  $\xi$ : lower moments, which weight typical rather than rare configurations, are *more* suppressed deep in the throat. Within this family, the breakdown of mean-field therefore cannot resurrect confinement; what it relaxes is the specific  $L^{-2}$  power, which should be read as an exact statement about the annealed  $\Delta = 1$  geometry.

*Isotropy, the  $2\zeta$  dictionary, and what is calibrated rather than predicted.* Two further structural choices enter (6)–(9) and deserve to be explicit. First, the isotropy of the Weyl factor — the same  $h$  multiplying  $dt^2$  and  $d\zeta^2$  — involves no loss of generality: every static two-dimensional metric is conformally flat, so isotropy is a choice of frame. The physical input is the choice of conformal frame itself, made by applying the *classical* geodesic dictionary — a boundary bilocal of separation  $\Delta t$  probes maximal Poincaré depth  $\zeta = \Delta t/2$  — to the *quantum* kernel,  $h(\zeta) \propto \zeta^2 G_{\partial\partial}(2\zeta)$ . An  $\mathcal{O}(1)$  rescaling of this dictionary,  $\Delta t = 2\zeta/\lambda$ , acts as  $\zeta \rightarrow \lambda\zeta$ , i.e. as a redefinition of  $C$ . The scaling exponents central to the rectangular-loop analysis — the  $\xi^{1/2}$  growth of  $h$ , the monotone decay of  $\mathcal{G}_0$ , and the  $L^{-2}$  screening law — are invariant under this rescaling, but calibrated scales are not: the crossover  $L_c^{\text{match}} = 82.4685C$ , the self-dual depth  $\zeta_{\text{sd}} = \pi C$ , and the coefficient  $\kappa_{\text{IR}}$  of (108) all shift, and should be quoted as prescription-calibrated quantities rather than invariant predictions.

Second, the transverse metric: as emphasized in Sec. 4.4,  $h$  dresses  $g_{tt}$  and  $g_{UU}$  but not  $g_{xx}$ , whose  $T^3$  volume sits in the dilaton sector of the reduction. Since the screening exponent follows from  $g_{tt}$  *together with* the  $\zeta$ -independence of  $g_{xx}$ , an independent quantum dressing of the dilaton sector could shift the exponent; this — not the isotropy of the AdS<sub>2</sub> factor — is the main structural assumption beyond mean-field, inherited from the matching ansatz of [24]. Finally, the bilocal-as-metric construction repackages averaged boundary-anchored geodesic data as an effective line element; gauge-invariant formulations of bulk observables and matter Wilson lines in JT gravity [17, 22, 42] and the ensemble treatment of the near-extremal spectrum [16, 23] provide the natural framework for going beyond it. The fully averaged observable  $\langle W \rangle$  itself — the Schwarzian average of the worldsheet functional, with the connected kernels of (51) evaluated at split arguments — is an interesting problem that we leave for future work.

In summary, the averaged-metric prescription is quantitatively controlled for  $\zeta \lesssim C$ , where  $\mathcal{V}(\xi) \approx \frac{2}{3}\xi \ll 1$  and the mean geometry is a faithful proxy for the typical one. Deep in the throat the kernel is fluctuation-dominated, and the rectangular-loop results of Sec. 4 should be read as statements about the annealed mean geometry: their qualitative content — monotone tension decay, absence of a confining wall, screening rather than confinement — is robust across the moment family by Proposition 2, while quantitative coefficients and the precise  $L^{-2}$  power are tied to the  $\Delta = 1$  prescription. The variance (54), being itself exactly Mordell, makes this error budget computable rather than conjectural.

## 4 Rectangular Wilson loop and the quark-antiquark potential

We now study the temporal rectangular Wilson loop in the quantum-corrected metric (9), within the same averaged-metric probe approximation adopted in [24] and following the general framework of [3, 4, 36, 37, 48]. We first derive the parametric integrals for the quark separation  $L$  and the static energy  $E$ , perform the standard ultraviolet (UV) subtraction, and then use the exact integral representation of  $h(\zeta)$  to determine the large-distance behavior of the quark-antiquark potential.

### 4.1 Parametric formulas and renormalization

We now consider a temporal rectangular Wilson loop extended for a time interval  $T$  (eventually  $T \rightarrow \infty$ ) and with spatial separation  $L$  between the quark and antiquark. In the quantum-corrected metric (9), choosing worldsheet coordinates  $\tau = t$ ,  $\sigma = x$ , and an embedding  $U = U(x)$ , the induced metric leads to the Nambu–Goto action [36]

$$S_{\text{NG}} = \frac{T}{2\pi} \int_{-L/2}^{L/2} dx \sqrt{h(U)^2 (\partial_x U)^2 + \frac{U^4}{R^4} f(U) h(U)}. \quad (60)$$

There is a conserved quantity associated with translations in  $x$ . Introducing  $v \equiv U/U_0$  and the shorthand  $f_v(v) = f(U_0 v)$ ,  $h_v(v) = h(U_0 v)$ , one finds that the separation  $L$  and the static

energy  $E = S_{\text{NG}}/T$  can be written as parametric integrals in terms of  $v$ :

$$\frac{L}{2} = \frac{R^2}{U_0} \int_1^\infty dv \frac{\sqrt{h_v(v)}}{v^2 \sqrt{f_v(v)}} \sqrt{\frac{f_v(1)h_v(1)}{v^4 f_v(v)h_v(v) - f_v(1)h_v(1)}}, \quad (61)$$

$$E = \frac{U_0}{\pi} \left[ \int_1^\infty dv \left( \frac{v^2 h_v(v) \sqrt{f_v(v)h_v(v)}}{\sqrt{v^4 f_v(v)h_v(v) - f_v(1)h_v(1)}} - h_v(v) \right) - \int_{U_T/U_0}^1 dv h_v(v) \right]. \quad (62)$$

Eliminating  $U_0$  between  $L$  and  $E$  yields the quark-antiquark potential [36].

The connected worldsheet action in (61)–(62) contains the standard ultraviolet divergence associated with the infinite masses of the external sources [3, 4]. We regulate the radial integral by cutting off the geometry at  $U = U_{\text{max}}$  (equivalently  $\zeta = \epsilon \ll 1$  in the  $\text{AdS}_2$  coordinate), and define the renormalized potential by subtracting two straight strings. Writing the on-shell energy of the connected configuration as an integral over  $U$ ,

$$E_{\text{conn}}(U_{\text{max}}; U_0) = \frac{1}{\pi} \int_{U_0}^{U_{\text{max}}} dU \frac{h(U)}{\sqrt{1 - \frac{U_0^4 f(U_0)h(U_0)}{U^4 f(U)h(U)}}}, \quad (63)$$

where  $U_0$  is the turning point. A straight string at fixed  $\vec{x}$  has induced metric  $\gamma_{tt} = g_{tt}$  and  $\gamma_{UU} = g_{UU}$ , hence

$$\sqrt{\det \gamma} = \sqrt{g_{tt}g_{UU}} = \alpha' h(U), \quad (64)$$

so the regulated mass of a single external source is

$$m_W(U_{\text{max}}) = \frac{1}{2\pi} \int_{U_T}^{U_{\text{max}}} dU h(U), \quad 2m_W(U_{\text{max}}) = \frac{1}{\pi} \int_{U_T}^{U_{\text{max}}} dU h(U). \quad (65)$$

We therefore define the renormalized potential by

$$E(U_0) \equiv \lim_{U_{\text{max}} \rightarrow \infty} \left( E_{\text{conn}}(U_{\text{max}}; U_0) - 2m_W(U_{\text{max}}) \right). \quad (66)$$

Using (63)–(65) one can rearrange the difference *exactly* as

$$E(U_0) = \frac{1}{\pi} \int_{U_0}^\infty dU \left[ \frac{h(U)}{\sqrt{1 - \frac{U_0^4 f(U_0)h(U_0)}{U^4 f(U)h(U)}}} - h(U) \right] - \frac{1}{\pi} \int_{U_T}^{U_0} dU h(U). \quad (67)$$

The first integral is UV-finite: at large  $U$  one has  $f(U) \rightarrow 1$  and  $h(U) \rightarrow 1$ , and the bracket admits the expansion

$$\frac{h(U)}{\sqrt{1 - \frac{U_0^4 f(U_0)h(U_0)}{U^4 f(U)h(U)}}} - h(U) = \frac{U_0^4 f(U_0)h(U_0)}{2U^4} + O(U^{-6}), \quad (68)$$

which is integrable at  $U = \infty$ .

To display the cancellation in the  $\zeta$ -cutoff language, use the near-boundary series  $h(\zeta) = 1 + O((\zeta/C)^2)$  from Eq. (8) and the matching relation  $U - U_T = R^2/(12\zeta)$  (Eq. (4)), so that  $dU = -(R^2/12) d\zeta/\zeta^2$ . The UV cutoff  $U_{\max}$  maps to a small  $\zeta$ -cutoff  $\epsilon > 0$ , and the integral from some finite  $U$  to the cutoff becomes

$$\int^{U_{\max}} dU h(U) = \frac{R^2}{12} \int_{\epsilon}^{\zeta_{\text{fin}}} \frac{d\zeta}{\zeta^2} [1 + O((\zeta/C)^2)] = \frac{R^2}{12} \left( \frac{1}{\epsilon} + O(1) \right), \quad (69)$$

where  $\zeta_{\text{fin}}$  is a fixed finite value (set by  $U_T$  or  $U_0$ ) that does not contribute to the divergence. Since both  $E_{\text{conn}}(U_{\max}; U_0)$  and  $2m_W(U_{\max})$  contain the same  $1/\epsilon$  pole, (66) is finite. The renormalized potential (67) receives contributions of competing sign: the first integral is positive while the subtraction term is negative. Both contribute at the same  $\zeta_0^{-1/2}$  order in the deep IR; the full numerical coefficient of the leading deep-IR behavior is therefore determined only after combining both terms in the throat analysis (Sec. 4.4). Combining the two throat contributions gives a negative overall coefficient (confirmed numerically in Sec. 4.5, where  $E < 0$  throughout the sampled branch); the subtraction term provides the simplest way to exhibit the scaling:

$$E(U_0) \sim -\frac{1}{\pi} \int_{U_T}^{U_0} dU h(U) < 0. \quad (70)$$

Using the asymptotic (24) together with  $U - U_T \propto \zeta^{-1}$  in the AdS<sub>2</sub> throat (Eq. (4)), one has

$$h(U) \sim A(U - U_T)^{-1/2} \quad (U \rightarrow U_T^+), \quad (71)$$

and therefore

$$E(U_0) \sim -\frac{A}{\pi} \int_0^{U_0 - U_T} dw w^{-1/2} = -\frac{2A}{\pi} \sqrt{U_0 - U_T} \propto -\zeta_0^{-1/2}, \quad (72)$$

where  $\zeta_0$  is the turning point in AdS<sub>2</sub> coordinates. A detailed turning-point derivation, establishing the relation  $L \propto \zeta_0^{1/4}$  and hence  $E(L) \propto -L^{-2}$ , is given in Sec. 4.4.

## 4.2 Short distances: Coulomb, analytic series, and nonperturbative corrections

At short distances the turning point  $U_0$  lies far from the horizon,  $h \rightarrow 1$ , and the standard conformal Coulomb result [3, 4] is recovered:

$$E(L) \underset{L \rightarrow 0}{\sim} -\kappa \frac{R^2}{L}, \quad \kappa = \frac{4\pi^2}{\Gamma(1/4)^4} \simeq 0.2285. \quad (73)$$

As  $L$  grows and the turning point enters the near-horizon region, the quantum corrections encoded in  $h(\zeta)$  deform this Coulomb tail. The exact integral representation implies the following structure for the small- $L$  expansion of the potential, generalizing the analysis of [24]:

$$E(L) = -\kappa \frac{R^2}{L} + \sigma_{\text{rect}} \frac{R^2}{C^2} L + \gamma_3 \frac{R^2}{C^4} L^3 + \gamma_5 \frac{R^2}{C^6} L^5 + \dots + \delta_{\text{mod}}(L). \quad (74)$$

The polynomial part is determined entirely by the near-boundary expansion (16). In the smooth matched ansatz (109), the leading short-distance deformation is fixed by

$$h(U) = 1 + \frac{\beta}{U^2} + O(U^{-3}), \quad \beta = \frac{c_2}{144} = \frac{1}{8640}, \quad (75)$$

where  $\xi = 1/[12(U - U_T)]$  and  $U_T = R = C = 1$ . Expanding the parametric integrals to first order in  $\beta/U_0^2$  gives a matched-ansatz calibration of the linear coefficient. With

$$I_0 := \int_1^\infty \frac{dv}{v^2 \sqrt{v^4 - 1}}, \quad \ell_0 := 2I_0, \quad (76)$$

$$I_1 := \frac{1}{2} \int_1^\infty \frac{dv}{v^2 \sqrt{v^4 - 1}} \left( 1 + \frac{1}{v^2} - \frac{1}{v^2 + 1} \right), \quad (77)$$

one finds

$$\sigma_{\text{rect}}^{\text{match}} = \frac{c_2}{144} \left( \frac{2I_1}{\pi \ell_0} + \frac{1}{4\pi} \right) = 3.3593845 \times 10^{-5}. \quad (78)$$

This is the term that, in finite-order analyses such as [24], is identified with a string tension reminiscent of the Cornell potential [33–35]. Its value is not universal: it is a calibration of the chosen matching prescription, whereas the  $L^{-2}$  tail below is fixed by the exact throat.

Our refined expansion (74) is consistent with the short-distance matching, but the linear term is not fundamental. Higher analytic corrections modify the Cornell form [33, 34] outside the strict UV regime, and at large distances the potential crosses over to the screened regime derived in the next subsection.

The correction  $\delta_{\text{mod}}(L)$  represents the effect of exponentially suppressed terms of order  $e^{-\pi^2 C/\zeta}$  in  $h(\zeta)$ , which arise from the  $S$ -transformed ( $q^*$ ) channel of the Mordell evaluation (Sec. 3.3, Eq. (43)) and are invisible to any finite Taylor truncation in  $\zeta/C$ . Their structure in terms of the Appell–Lerch sums  $L_r(q^*)$  is made explicit by the  $q^*$ -dependent terms in (43), but the precise functional form of  $\delta_{\text{mod}}$  as a function of  $L$  depends on the mapping between the AdS<sub>2</sub> coordinate  $\zeta$  and the boundary separation  $L$ , which in turn relies on the matching of the near-horizon and far metrics [24]; its determination is left for future work. The exponential scale  $e^{-\pi^2 C/\zeta}$  is connected to the optimal truncation of the asymptotic near-boundary series (Sec. 3.1): at order  $m_{\text{opt}} \sim \pi^2/\xi$  the truncation error is minimized, and the remaining irreducible error is precisely of the modular/nonperturbative order  $q^* = e^{-\pi^2/\xi}$ .

### 4.3 Long distances: algebraic screening

From the deep-interior asymptotic (24), the AdS<sub>2</sub> warp factor behaves for  $\zeta \gg C$  as

$$a(\zeta) := \frac{L_2^2}{\zeta^2} h(\zeta) \sim \frac{A}{\zeta^{3/2}}, \quad A > 0. \quad (79)$$

This is the only input needed to determine the long-distance Wilson-loop tail. A detailed turning-point analysis (Sec. 4.4) shows that  $L \propto \zeta_0^{1/4}$  and  $E \propto -\zeta_0^{-1/2}$ , giving the algebraically screened regime

$$E(L) \sim -\frac{\kappa_{\text{IR}}}{L^2}, \quad F(L) = -\frac{dE}{dL} \sim -\frac{2\kappa_{\text{IR}}}{L^3}, \quad L \gg C. \quad (80)$$

In particular, the potential vanishes as  $L \rightarrow \infty$  and approaches zero from below. Thus the deep IR does not enforce a transition to disconnected worldsheets; any Gross–Ooguri-type transition [49] (if present) would have to arise from intermediate scales. The numerical check of Sec. 4.5 finds no such pre-emption in the minimal smooth matched ansatz. At any nonzero temperature one expects the familiar screening transition to reappear.

The physical interpretation of (80) is therefore sharper than the exponent alone. The extremal RN brane is governed in the IR by the  $\text{AdS}_2 \times \mathbb{R}^3$  semi-local quantum liquid: the time direction is critical, while the spatial directions are spectators of the  $z \rightarrow \infty$  scaling [7, 8]. A thermal plasma with a finite screening mass would give a Debye tail, schematically  $E_{\text{conn}}(L) \sim \exp[-m_D(T)L]$ , or a connected branch pre-empted by a disconnected saddle. By contrast, the infinitely long extremal throat supplies no thermal cap, and the connected string samples a scale-free IR geometry; the result is the power-law screening  $E(L) \propto -L^{-2}$ . In this sense the algebraic tail is a sharp Wilson-loop diagnostic of the semi-local critical IR, while the expected exponential screening at any  $T > 0$  is the corresponding diagnostic that the critical throat has been cut off.

*Absence of the mass gap.* The  $L^{-2}$  screening forces a reinterpretation of the “mass gap” reported in the truncated analysis of [24]. In the truncated perturbative treatment, the confinement indicator  $\mathcal{G}_0(\zeta) := h(\zeta)/\zeta^2$  (following [24]) develops a minimum at finite radial depth (Fig. 8), and the curvature of the effective potential at this minimum defines a characteristic mass scale  $m_{\text{gap}}$  for radial string fluctuations. In the exact throat geometry, this minimum is absent:  $\mathcal{G}_0$  decays monotonically as  $\zeta^{-3/2}$  and the effective string tension  $\mathcal{T}(\zeta) \propto \zeta^{-3/4}$  decreases monotonically toward zero as the string descends into the  $\text{AdS}_2$  throat (see Sec. 4.4 below). There is consequently no stable minimum around which bound-state fluctuations could be quantized, and no evidence for a discrete gapped tower of radial string excitations in the exact throat analysis. The scale previously identified as  $m_{\text{gap}}$  retains a weaker meaning: it corresponds to the curvature scale of the effective potential at the crossover region where the approximately linear plateau gives way to the screened regime. The monotone decay of the effective string tension reflects the gapless nature of the extremal horizon [14], strongly modified by the quantum corrections encoded in the scaling (24) deep in the throat.

*Analytic proof of monotone decay.*

**Theorem 3** (Complete monotonicity of the confinement indicator). *The confinement indicator  $\mathcal{G}_0(\xi) := h(\xi)/\xi^2$  is completely monotone on  $(0, \infty)$  in the sense of Bernstein [50]: for every integer  $n \geq 0$ ,*

$$(-1)^n \mathcal{G}_0^{(n)}(\xi) = 2 \int_0^\infty dy y^{3+2n} e^{-\xi y^2} \coth(\pi y) > 0, \quad \xi > 0. \quad (81)$$

*In particular,  $\mathcal{G}_0$  is strictly positive and strictly decreasing, and admits no finite- $\xi$  minimum.*

*Proof.* From the exact integral representation (15),

$$\mathcal{G}_0(\xi) = \frac{h(\xi)}{\xi^2} = 2 \int_0^\infty dy y^3 e^{-\xi y^2} \coth(\pi y). \quad (82)$$

The integrand  $y^3 e^{-\xi y^2} \coth(\pi y)$  is strictly positive for all  $y > 0$  and  $\xi > 0$ , and the integral converges absolutely, so  $\mathcal{G}_0(\xi) > 0$ . Differentiation under the integral sign (justified by the Gaussian decay) gives

$$\mathcal{G}'_0(\xi) = -2 \int_0^\infty dy y^5 e^{-\xi y^2} \coth(\pi y) < 0 \quad \text{for all } \xi > 0, \quad (83)$$

and more generally, the  $n$ -th derivative brings down  $(-y^2)^n$ , yielding (81) with a manifestly positive integrand.  $\square$

**Remark 4.** *In the notation of Kinar, Schreiber, and Sonnenschein [36], the temporal effective string tension satisfies  $f_{\text{string}}^2 = g_{tt}g_{xx} \propto h(\zeta)/\zeta^2 = \mathcal{G}_0(\zeta)$ . Using  $s = U - U_T \sim \zeta^{-1}$  one has  $f_{\text{string}}(s) \sim s^{3/4}$ , so  $f_{\text{string}}(0) = 0$ . Thus the exact throat belongs to the Kinar–Schreiber–Sonnenschein nonconfining power-law branch, not the  $f(0) > 0$  confining branch. Complete monotonicity of  $\mathcal{G}_0$  means that no finite-depth positive minimum of  $f_{\text{string}}$  can arise, ruling out confinement at the level of the exact throat geometry.*

*Prescription robustness.* Theorem 3 is a statement about the mean ( $\Delta = 1$ , annealed) geometry. Proposition 2 of Sec. 3.5 extends the decisive part — strict monotone decay of the confinement indicator, hence the absence of any finite-depth minimum — to the full family of moment-based effective geometries  $h_\Delta^{1/\Delta}$ , so the identification of the confining minimum as a truncation artifact does not rest on the averaged-metric choice. The quantitative reach of the mean geometry itself is delimited by the exact variance (54): relative kernel fluctuations reach unity at  $\xi \simeq 1.22$  and grow as  $(\sqrt{\pi}/3) \xi^{3/2}$  beyond, so the  $-\kappa_{\text{IR}}/L^2$  law is the exact screening law of the annealed geometry, with the prescription dependence of the exponent quantified in Sec. 3.5.

## 4.4 Detailed derivation of the IR scaling

The deep-infrared tail  $E(L) \sim -\kappa_{\text{IR}}/L^2$  follows from a systematic turning-point expansion of the Wilson-loop parametrics [36, 37]. We present this derivation in two complementary forms: (i) a pure  $\zeta$ -coordinate analysis in the AdS<sub>2</sub> throat, and (ii) an effective-tension formulation that isolates the geometric origin of the exponents.

*Pure  $\zeta$ -coordinate derivation.*

In the near-horizon region, the geometry is AdS<sub>2</sub>  $\times$   $T^3$  with quantum-corrected AdS<sub>2</sub> factor (cf. Sec. 2):

$$ds_{\text{throat}}^2 \approx h(\zeta) \frac{L_2^2}{\zeta^2} (dt^2 + d\zeta^2) + \ell_x^2 d\vec{x}^2, \quad \ell_x^2 := \frac{u_T^2}{L_{\text{AdS}}^2}. \quad (84)$$

We compute the rectangular Wilson loop using worldsheet coordinates  $\tau = t$ ,  $\sigma = x$  and embedding  $\zeta = \zeta(x)$ .

The induced metric gives the Euclidean Nambu–Goto density  $\mathcal{L} = \sqrt{g_{tt}} \sqrt{g_{xx} + g_{\zeta\zeta} \zeta'^2}$  [36]. Because  $\mathcal{L}$  has no explicit  $x$ -dependence, the conserved first integral gives

$$\frac{dx}{d\zeta} = \frac{L_2}{\ell_x} \frac{\sqrt{h(\zeta)}}{\zeta} \frac{1}{\sqrt{\frac{h(\zeta)\zeta_0^2}{h(\zeta_0)\zeta^2} - 1}}. \quad (85)$$

In the deep interior,  $h(\zeta) \simeq a \zeta^{1/2}$  with  $a > 0$ , so  $\sqrt{h(\zeta)} \simeq \sqrt{a} \zeta^{1/4}$  and

$$\frac{h(\zeta)\zeta_0^2}{h(\zeta_0)\zeta^2} \simeq \frac{a\zeta^{1/2}\zeta_0^2}{a\zeta_0^{1/2}\zeta^2} = \left(\frac{\zeta_0}{\zeta}\right)^{3/2}. \quad (86)$$

Plugging into (85) and rescaling  $\zeta = \zeta_0 u$ ,

$$\begin{aligned} \frac{L}{2} &\simeq \frac{L_2\sqrt{a}}{\ell_x} \int_0^{\zeta_0} d\zeta \frac{\zeta^{-3/4}}{\sqrt{\left(\frac{\zeta_0}{\zeta}\right)^{3/2} - 1}} \\ &= \frac{L_2\sqrt{a}}{\ell_x} \zeta_0^{1/4} \int_0^1 du \frac{1}{\sqrt{1 - u^{3/2}}}. \end{aligned} \quad (87)$$

The remaining integral is a Beta function:

$$\int_0^1 \frac{du}{\sqrt{1 - u^{3/2}}} = \frac{2}{3} B\left(\frac{2}{3}, \frac{1}{2}\right) = 4\sqrt{\pi} \frac{\Gamma(2/3)}{\Gamma(1/6)}. \quad (88)$$

Hence the scaling is explicit:

$$L \propto \zeta_0^{1/4}. \quad (89)$$

The force on the quark-antiquark pair is  $F(L) = -dE/dL$ , where

$$-F(L) = \frac{1}{2\pi} \sqrt{g_{tt}g_{xx}} \Big|_{\zeta_0} = \frac{1}{2\pi} \frac{L_2}{\zeta_0} \sqrt{\ell_x^2 h(\zeta_0)}. \quad (90)$$

With  $h(\zeta_0) \sim a\zeta_0^{1/2}$  this gives  $|F| \propto \zeta_0^{-3/4}$ . Using  $L \propto \zeta_0^{1/4} \Rightarrow \zeta_0 \propto L^4$ , we obtain

$$F(L) \propto -L^{-3} \quad \Rightarrow \quad E(L) \propto -L^{-2}, \quad (91)$$

consistent with the algebraic screening regime.

*Effective-tension viewpoint.*

The scaling can be understood directly by introducing the *local effective string tension* [36]

$$\mathcal{T}(\zeta) := \frac{1}{2\pi\alpha'} \sqrt{g_{tt}(\zeta) g_{xx}} \propto \sqrt{g_{tt}(\zeta) g_{xx}}. \quad (92)$$

Since  $g_{xx} = \ell_x^2$  is constant in the throat and  $g_{tt} = L_2^2 h(\zeta)/\zeta^2$ , we have

$$\mathcal{T}(\zeta) \propto \frac{\sqrt{h(\zeta)}}{\zeta}. \quad (93)$$

The conserved quantity from  $x$ -translations can be recast as

$$\frac{dx}{d\zeta} = \sqrt{\frac{g_{\zeta\zeta}}{g_{xx}}} \frac{1}{\sqrt{\left(\frac{\mathcal{T}(\zeta)}{\mathcal{T}(\zeta_0)}\right)^2 - 1}}, \quad \frac{L}{2} = \int_0^{\zeta_0} d\zeta \frac{dx}{d\zeta}. \quad (94)$$

This is the “effective potential” form:  $\zeta'(x)^2$  is controlled by the ratio  $\mathcal{T}(\zeta)/\mathcal{T}(\zeta_0)$ , and the turning point occurs where the bracket vanishes.

Because of the AdS<sub>2</sub> throat (double zero of  $f$ ), we have the universal relation  $g_{tt} = g_{\zeta\zeta} \propto h(\zeta)/\zeta^2$ . For the deep-IR asymptotic  $h(\zeta) \sim \zeta^a$ , this gives

$$g_{tt}(\zeta) \propto \frac{h(\zeta)}{\zeta^2} \sim \zeta^{a-2} \equiv \zeta^{-p}, \quad p := 2 - a, \quad (95)$$

and from (93),  $\mathcal{T}(\zeta) \propto \zeta^{-p/2}$ . Evaluating (94) with  $g_{\zeta\zeta} = g_{tt} \sim \zeta^{-p}$  and  $g_{xx} = \ell_x^2$ , and rescaling  $\zeta = \zeta_0 u$ , one finds

$$L \propto \zeta_0^{1-p/2} = \zeta_0^{a/2}. \quad (96)$$

Thus the exponent in  $L(\zeta_0)$  is fixed entirely by the single IR power of  $h(\zeta)$  together with AdS<sub>2</sub> scaling (which enforces the  $\zeta^{-2}$  factor in  $g_{tt}$ ).

In the present problem,  $a = \frac{1}{2}$  and  $p = \frac{3}{2}$ , giving immediately

$$L \propto \zeta_0^{1/4}, \quad \mathcal{T}(\zeta) \propto \zeta^{-3/4}. \quad (97)$$

The effective tension decreases monotonically as the string descends deeper into the throat, with no minimum—this is the geometric origin of the absence of a confining regime. A common AdS<sub>2</sub> intuition [3] is that for a metric of the form  $ds^2 \sim (dx^2 + d\zeta^2)/\zeta^2$  one finds a turning-point relation  $L \propto \zeta_0$  (the geodesic “semicircle” picture), which would suggest that an estimate of the form  $E \sim L \mathcal{G}_0(\zeta_0)$  with  $\mathcal{G}_0 = h(\zeta)/\zeta^2$  leads to a fractional power law  $E(L) \sim L^{-1/2}$  when  $h(\zeta) \sim (\zeta/C)^{1/2}$ . However, this reasoning does *not* apply in the present background: in the AdS<sub>2</sub>  $\times$   $T^3$  throat (84) the separation directions lie in the transverse  $T^3$  factor, so  $g_{xx}$  is  $\zeta$ -independent, and in the full string-frame metric (9) the quantum factor  $h$  multiplies  $g_{tt}$  and  $g_{UU}$  but *not*  $g_{xx}$ .

## 4.5 Numerical check of the connected branch in a smooth matched ansatz

The preceding derivation establishes the local deep-throat saddle. A separate question, familiar from holographic Wilson-loop analyses, is whether this saddle lies on the physical branch of the global parametric curve. In particular, multi-branch structure can occur when the string probes different radial regimes, and the physical branch must satisfy the usual monotonicity and concavity conditions

$$\frac{dL}{dU_0} < 0, \quad \frac{dE}{dL} > 0, \quad \frac{d^2E}{dL^2} \leq 0, \quad (98)$$

where  $U_0$  is the turning point in a radial coordinate increasing toward the asymptotic AdS<sub>5</sub> boundary. (The condition  $dE/dL > 0$  is consistent with the attractive force  $F(L) = -dE/dL < 0$ ; note that  $E(L) < 0$  and approaches zero from below, so  $E$  is an increasing function of  $L$  in the screened regime.) Equivalently, in the notation of the stability analyses of classical string embeddings, a branch with the opposite sign of  $dL/dU_0$  is a natural candidate for a fluctuation instability [51, 52]. Examples with several competing branches, maximal separations, or first-order branch changes have been studied in related D3-brane

geometries [53]; recent Wilson-loop computations also emphasize the usefulness of global numerical minimization when conformal, confining, and screened regimes coexist [54].

We therefore performed a direct numerical check (full implementation details, tolerances, and cutoff-dependence tests are collected in Appendix A) using the exact integral representation of  $h$ . First, in the pure AdS<sub>2</sub> throat, the result can be packaged as a universal normalized screening curve. In units  $C = L_2 = \ell_x = 1$ , with the boundary condition  $h(0) = 1$  fixed as in (15), the separation and renormalized energy are

$$L_{\text{th}}(\xi_0) = 2 \int_0^1 du \left( \frac{h_0 h(\xi_0 u)}{h(\xi_0 u) - h_0 u^2} \right)^{1/2}, \quad (99)$$

$$E_{\text{th}}(\xi_0) = \frac{1}{\pi} \left[ \frac{1}{\xi_0} \int_0^1 du \frac{h(\xi_0 u)}{u^2} \left( \frac{1}{\sqrt{1 - h_0 u^2/h(\xi_0 u)}} - 1 \right) - \int_{\xi_0}^{\infty} d\xi \frac{h(\xi)}{\xi^2} \right], \quad (100)$$

where  $h_0 := h(\xi_0)$ . The endpoint singularity in (100) is integrable and was treated by a change of variables in the numerical code. Equations (99)–(100) should be read as more than a numerical check: they define a reusable universal function, independent of the UV completion,

$$\mathfrak{E}_{\text{th}}(\mathfrak{L}) := E_{\text{th}}(\xi_0(\mathfrak{L})), \quad \mathfrak{L} := L_{\text{th}}(\xi_0), \quad \xi_0 \in (0, \infty). \quad (101)$$

This curve has an exact short-endpoint structure. If the throat is classical,  $h \equiv 1$ , then

$$L_{\text{th}} = 2 \int_0^1 \frac{du}{\sqrt{1 - u^2}} = \pi, \quad E_{\text{th}} = 0, \quad (102)$$

for every turning point: the connected and disconnected saddles are marginally degenerate at the single separation  $\mathfrak{L} = \pi$ . The full Schwarzian curve is therefore quantum-generated. As  $\xi_0 \rightarrow 0$ , one finds

$$\mathfrak{E}_{\text{th}}(\pi) = -\frac{1}{\pi} \int_0^{\infty} d\xi \frac{h(\xi) - 1}{\xi^2} = -\frac{1}{6\pi}, \quad (103)$$

where the last equality follows directly from

$$\int_0^{\infty} d\xi \frac{h(\xi) - 1}{\xi^2} = 4 \int_0^{\infty} \frac{y dy}{e^{2\pi y} - 1} = \frac{4\zeta_{\text{R}}(2)}{(2\pi)^2} = \frac{1}{6}. \quad (104)$$

Numerically  $\mathfrak{L} - \pi = O(\xi_0^2)$  while  $\mathfrak{E}_{\text{th}} + 1/(6\pi) = O(\xi_0)$ , so the pure-throat curve leaves the threshold with a square-root branch point. In the isolated throat  $\mathfrak{L} = \pi$  is a minimal separation; in a matched AdS<sub>5</sub>/AdS<sub>2</sub> geometry, smaller separations are supplied by the far-region branch.

Restoring units for any geometry whose connected string enters the same Schwarzian throat gives

$$L = \frac{L_2}{\ell_x} \mathfrak{L}, \quad E = \frac{L_2^2}{C} \mathfrak{E}_{\text{th}}(\mathfrak{L}), \quad (105)$$

with all model dependence confined to the matching onto this curve and to the identification of  $C$ ,  $L_2$ , and  $\ell_x$ . At the threshold,  $E_{\text{th}} = -L_2^2/(6\pi C)$ ; this binding energy vanishes in the

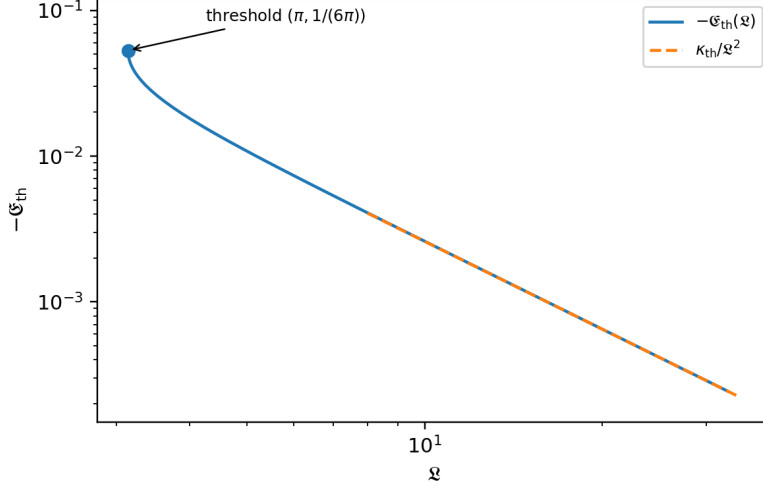


**Figure 5:** Universal throat screening curve in the normalized units  $C = L_2 = \ell_x = 1$ . The plotted quantity is  $-\mathfrak{E}_{\text{th}}(\mathfrak{L})$ . The left endpoint is the exact quantum threshold  $(\mathfrak{L}, -\mathfrak{E}_{\text{th}}) = (\pi, 1/(6\pi))$ ; the dashed line is the large-separation tail  $\kappa_{\text{th}}/\mathfrak{L}^2$ .

classical limit  $C \rightarrow \infty$ . The large- $\mathfrak{L}$  endpoint of the universal function is the semi-local screening law  $\mathfrak{E}_{\text{th}}(\mathfrak{L}) \sim -\kappa_{\text{th}}/\mathfrak{L}^2$ . These formulae give

$$(-E_{\text{th}})L_{\text{th}}^2 = 0.26003 \quad (\xi_0 > 10^3), \quad \frac{d \log(-E_{\text{th}})}{d \log L_{\text{th}}} = -2.001, \quad (106)$$

which agrees with the analytic coefficient

$$\kappa_{\text{th}} = \frac{32}{\sqrt{\pi}} \left( \frac{\Gamma(2/3)}{\Gamma(1/6)} \right)^3 = 0.259920745 \dots \quad (107)$$

Figure 5 shows the full universal curve and both exact endpoints. In particular,  $(-\mathfrak{E}_{\text{th}})\mathfrak{L}^2$  runs from the threshold value  $\pi/6$  to  $\kappa_{\text{th}}$  as the turning point moves from the boundary to the deep throat.

Equivalently, the coefficient in physical units is

$$\kappa_{\text{IR}} = \frac{32}{\sqrt{\pi}} \left( \frac{\Gamma(2/3)}{\Gamma(1/6)} \right)^3 \frac{L_2^4}{\ell_x^2 C}. \quad (108)$$

Here  $L_2$  is the  $\text{AdS}_2$  radius (length),  $\ell_x = u_T/L_{\text{AdS}}$  is the dimensionless horizon scale entering the transverse metric, and  $C$  is the JT heat capacity (length), so  $\kappa_{\text{IR}}$  has dimensions of [length], consistent with  $E(L) \sim -\kappa_{\text{IR}}/L^2$  for a renormalized energy  $E$  of dimension [length] $^{-1}$ . (The normalized curve of Sec. 4.1 is obtained in units  $C = L_2 = \ell_x = 1$ , in which  $E$  and  $L$  are measured in the same length unit.)

Second, to check that the connected saddle remains dominant across the  $\text{AdS}_5/\text{AdS}_2$  interpolation, we used the minimal smooth completion

$$f(U) = 1 - \frac{3}{U^4} + \frac{2}{U^6}, \quad \xi(U) = \frac{1}{12C(U - U_T)}, \quad h(U) = h_{\text{exact}}(\xi(U)), \quad (109)$$

with  $U_T = R = C = 1$ . This ansatz is not a substitute for a first-principles solution of the quantum-corrected interpolation; it is the simplest smooth geometry that has the exact Schwarzsian throat in the IR and tends to  $h = 1$  in the UV. The parametric integrals of Sec. 4.1 were then evaluated over

$$U_0 - U_T \in [10^{-7}, 10^2]. \quad (110)$$

Over this range no cusp or maximal separation was found, and the sign conditions (111) hold (Fig. 6):

$$\frac{dL}{dU_0} < 0, \quad \frac{dE}{dL} > 0, \quad \frac{d^2E}{dL^2} < 0 \quad (111)$$

at every sampled point. Since the near-horizon radius of the extremal RN-AdS<sub>5</sub> throat in these units is  $L_2^2 = 1/12$ , Eq. (108) predicts

$$\kappa_{\text{RN}} = \frac{\kappa_{\text{th}}}{144} = 1.805005 \times 10^{-3}. \quad (112)$$

The numerical branch gives

$$\langle (-E)L^2 \rangle_{\xi_0 > 10^4} = 1.80408 \times 10^{-3}, \quad \frac{d \log(-E)}{d \log L} = -2.003, \quad (113)$$

confirming that, in this matched ansatz, the connected branch remains monotone, concave, and reaches the algebraically screened IR regime. With the subtraction convention in which the disconnected pair has zero energy, the numerical energy is negative throughout the sampled branch, so no disconnected saddle pre-empts it within this ansatz.

The conclusion of this numerical exercise (which used a logarithmic grid of 100 turning points over  $U_0 - U_T \in [10^{-7}, 10^2]$  with UV cutoff  $U_{\text{max}} = 10^4$ ) is deliberately modest but important: within the natural smooth completion (109), the screened saddle is not merely an asymptotic solution of the isolated throat. It lies on the same monotone, concave connected branch that emerges from the UV. A different conclusion would require a genuine feature of the unknown first-principles quantum-corrected matching region, not the exact throat asymptotics alone.

The same matched-ansatz computation gives a direct observable diagnostic of the pseudo-linear question. Define

$$n_F(L) := -\frac{d \log |F|}{d \log L}, \quad |F| = \frac{dE}{dL}. \quad (114)$$

The Coulomb, linear, and screened regimes correspond respectively to  $n_F = 2$ ,  $n_F = 0$ , and  $n_F = 3$ . Figure 7 compares the exact branch with the same matched ansatz evaluated using the  $\mathcal{O}(\xi^4)$  polynomial  $h^{(4)} = 1 + \xi^2/60 - \xi^3/126 + \xi^4/240$ . For the truncated polynomial the effective wall sits at

$$\xi_{\text{wall}} = 4.19169, \quad |F|_{\text{wall}} = 1.54314 \times 10^{-2}, \quad (115)$$

and the force exponent tends to  $n_F \rightarrow 0$ , producing a genuine linear asymptote inside the truncated geometry. In the exact geometry, by contrast, the force passes from the Coulomb law through a crossover and then approaches  $|F| = 2\kappa_{\text{RN}}/L^3$ ; it does not remain near  $n_F = 0$  over an extended interval. The approximately linear behavior obtained from  $h^{(4)}$  is therefore a finite-order truncation shoulder, not a stable intermediate phase of the exact matched branch.

## 4.6 Crossover scales and modular structure

The Coulomb coefficient  $\kappa$  is fixed by the AdS<sub>5</sub> asymptotics [3], while the linear coefficient  $\sigma_{\text{rect}}$  is induced by the Schwarzian/JT scale  $C$  [24]. In the smooth matched ansatz, Eq. (78) gives a numerical UV calibration. Equating the Coulombic and linear terms in (74) gives

$$L_c^{\text{match}} = \sqrt{\frac{\kappa}{\sigma_{\text{rect}}^{\text{match}}}} C = 82.4685 C. \quad (116)$$

Because this estimate uses only the first two UV terms, it should not be read as evidence for a real long plateau. It is a matching coefficient; the observable force comparison in Fig. 7 tests directly whether a constant-force region persists in the exact branch.

The exact integral representation provides two natural asymptotic channels controlled by the modular pair

$$\tau = \frac{i\zeta}{\pi C} = \frac{i\xi}{\pi}, \quad q \equiv e^{\pi i \tau} = e^{-\zeta/C} = e^{-\xi}, \quad q^* \equiv e^{-\pi i/\tau} = \exp\left(-\frac{\pi^2 C}{\zeta}\right) = \exp\left(-\frac{\pi^2}{\xi}\right). \quad (117)$$

The channel weights are comparable when  $|q| = |q^*|$ , which fixes the *self-dual point* of the modular inversion  $\xi \mapsto \pi^2/\xi$ :

$$|q| = |q^*| \iff \xi = \frac{\pi^2}{\xi} \iff \xi_{\text{sd}} = \pi \quad (\text{equivalently } \zeta_{\text{sd}} = \pi C). \quad (118)$$

Since the turning point  $\zeta_0$  increases monotonically with the boundary separation  $L$ , this gives a geometric definition of a boundary crossover length,

$$L_{\text{sd}} \equiv L(\zeta_0 = \zeta_{\text{sd}}) = L(\zeta_0 = \pi C). \quad (119)$$

Unlike (116), which is a coefficient-matching estimate,  $L_{\text{sd}}$  is fixed by the dual  $q$ - and  $q^*$ -expansion structure of the Mordell identity. The radial crossover depth  $\zeta_{\text{sd}} = \pi C$  is intrinsic to the modular structure; the associated boundary separation  $L_{\text{sd}}$ , however, still depends on the  $\zeta_0 \mapsto L$  map and hence on the matched geometry away from the throat. On the connected-string branch at extremality, the modular crossover is smooth, with no cusp or discontinuity in  $E(L)$  or the force  $F(L) = -dE/dL$ . In the approximately linear regime  $F \approx -\sigma_{\text{eff}}$ , while in the algebraic screening regime (80) one has  $F(L) \propto -L^{-3}$ ; the modular self-dual point  $L_{\text{sd}}$  provides a useful reference scale for this crossover, although the actual approach to the clean  $L^{-2}$  tail is broad and is determined by the full  $L(\zeta_0)$  map, as illustrated numerically in Sec. 4.5 for the minimal smooth matched ansatz.

To summarize, the single dimensionful scale  $C$  from the Schwarzian sector enters the physics in three distinct ways. First, the short-distance matching coefficient gives the UV calibration  $L_c^{\text{match}} = 82.4685 C$  (Sec. 4.2), which should not be confused with a robust plateau scale. Second, it controls the nonperturbative exponential corrections: the  $S$ -transformed channel of the Mordell integral produces exponentially suppressed corrections to  $h(\zeta)$  of order  $e^{-\pi^2 C/\zeta}$ , which are invisible to any finite Taylor truncation and represent a genuinely nonperturbative correction with respect to the  $\xi \rightarrow 0$  near-boundary power expansion. Third,  $C$  governs the crossover to infrared screening:  $L_{\text{sd}} = L(\zeta_0 = \pi C)$  provides a modular reference scale for the crossover toward the screened regime. All three crossovers are tied to a single physical origin: the quantum fluctuations of the Schwarzian boundary mode of JT gravity in the near-horizon AdS<sub>2</sub> region.

## 4.7 Limits of finite-order truncation

Standard perturbative analyses [24–26] rely on a Taylor expansion of the metric factor around the boundary ( $\zeta = 0$ ):

$$h_N(\zeta) = 1 + \sum_{k=2}^N a_k \left(\frac{\zeta}{C}\right)^k, \quad (120)$$

where the signed coefficients  $a_k$  are read off from the expansion (16) (e.g.  $a_2 = +1/60$ ,  $a_3 = -1/126$ ,  $a_4 = +1/240$ ). While this series provides a valid effective description for  $\zeta \ll C$ , it encounters structural limitations when extrapolated to the infrared ( $\zeta \gg C$ ).

For any truncation at even  $N > 2$ , the leading coefficient  $a_N > 0$  ensures that  $\mathcal{G}_{0,N}(\zeta) = h_N(\zeta)/\zeta^2$  diverges both as  $\zeta \rightarrow 0$  and as  $\zeta \rightarrow \infty$  (since  $h_N \sim \zeta^N$  at large  $\zeta$ ). By continuity,  $\mathcal{G}_{0,N}$  therefore possesses at least one global minimum at finite  $\zeta$ ; for the  $\mathcal{O}(\zeta^4)$  truncation this is the stationary point at  $\zeta \simeq 4.19$  shown in Fig. 8 (dashed curve). However, this feature lies well outside the domain where the truncated series is accurate (Fig. 2) and is thus an artifact of truncation.

By contrast, the exact solution (Eq. (24)) gives  $\mathcal{G}_0(\zeta) \sim \zeta^{-3/2}$ , which decays monotonically without any extremum. Finite-order extrapolations therefore artificially induce a spurious minimum where none exists in the exact throat geometry.

The exact integral representation

$$h(\zeta) = 2 \left(\frac{\zeta}{C}\right)^2 \int_0^\infty dy y^3 e^{-(\zeta/C)y^2} \coth(\pi y) \quad (121)$$

is equivalent to a Mordell transform (Sec. 3.3), evaluated explicitly in Eq. (43), and therefore exposes two complementary expansion parameters:  $q^* = e^{-\pi^2 C/\zeta}$ , small near the AdS<sub>2</sub> boundary ( $\zeta \ll C$ ), and  $q = e^{-\zeta/C}$ , small deep in the throat ( $\zeta \gg C$ ). In practice this provides a controlled interpolation between the two regimes.

- *UV expansion* ( $\zeta \ll C$ ): The near-boundary behavior (Sec. 3.1) contains the analytic power series in  $\zeta/C$  together with modular ( $S$ -transformed) terms of the form  $\sim \exp(-\pi^2 C/\zeta)$ , which are invisible to any finite truncation in powers of  $\zeta$ .
- *IR expansion* ( $\zeta \gg C$ ): In the deep interior the natural expansion variable is  $q = e^{-\zeta/C}$ . The exact integral (Sec. 3.2) gives

$$h(\zeta) \sim (\zeta/C)^{1/2} \left[ 1 + \mathcal{O}\left(\frac{C}{\zeta}\right) \right] + \mathcal{O}(e^{-\zeta/C}), \quad (122)$$

so that the leading  $\zeta^{1/2}$  scaling—and thus the monotone decay  $\mathcal{G}_0(\zeta) \sim \zeta^{-3/2}$ —is obtained directly from the exact nonperturbative completion rather than from any finite near-boundary truncation.

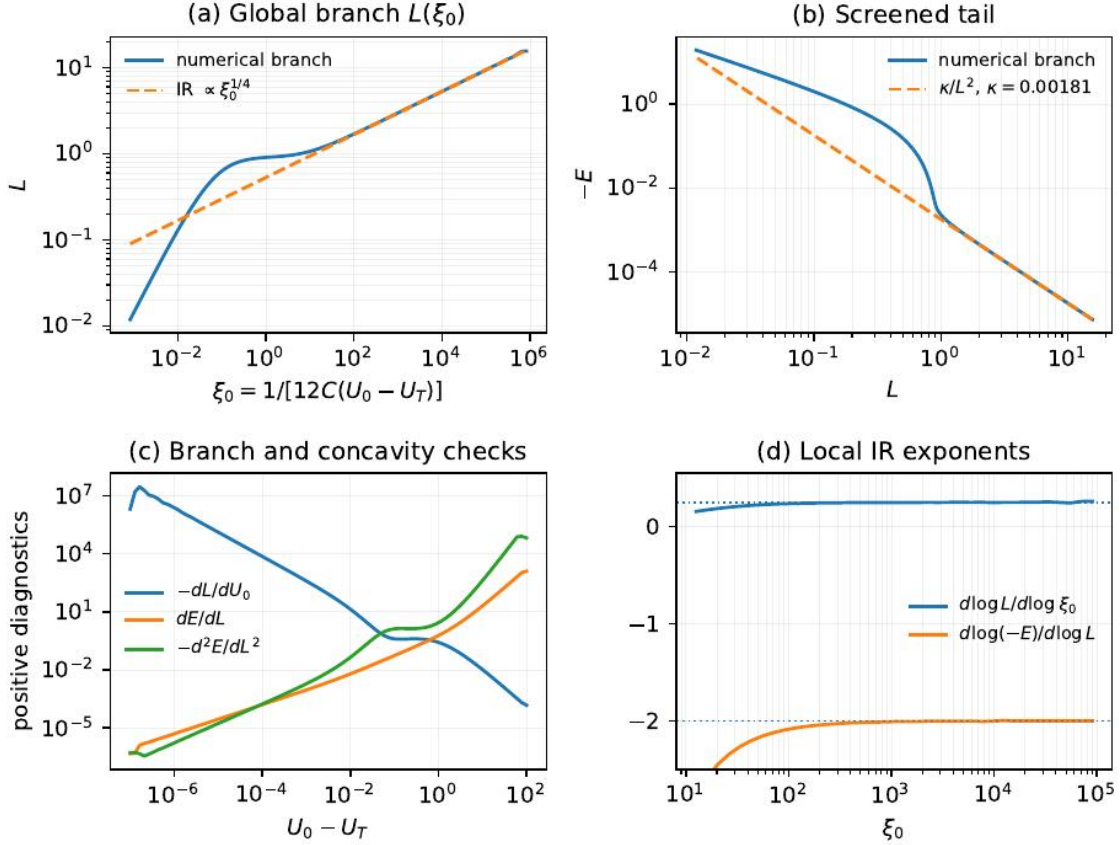


**Figure 6:** Numerical check of the connected branch using the exact metric factor  $h(\xi)$ . Panel (a) shows the global branch  $L(\xi_0)$  in the smooth matched ansatz (109); at large  $\xi_0$  it approaches the analytic  $\xi_0^{1/4}$  throat scaling. Panel (b) shows that the same branch approaches the screened tail  $-E = \kappa/L^2$  with  $\kappa = \kappa_{\text{th}}/144$ . Panel (c) plots the positive quantities  $-dL/dU_0$ ,  $dE/dL$ , and  $-d^2E/dL^2$ ; thus the branch satisfies the stability/concavity diagnostics throughout the sampled range. Panel (d) shows the local exponents approaching  $1/4$  and  $-2$ , respectively.

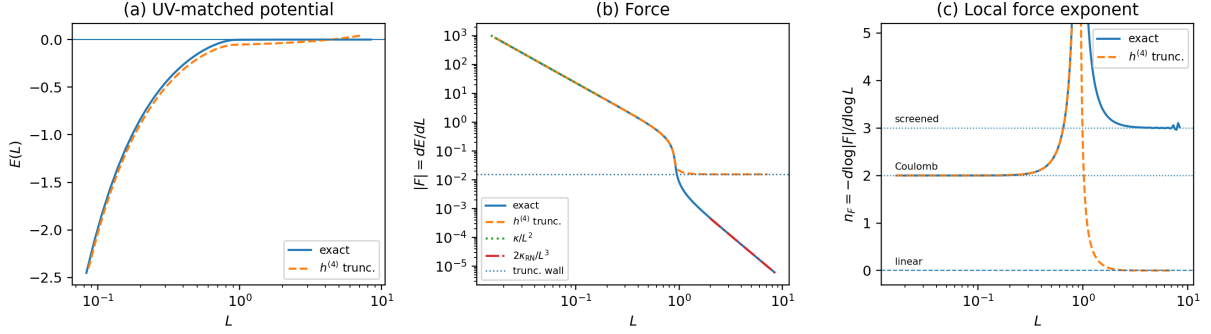


**Figure 7:** Observable-level comparison between the exact Schwarzian metric factor and the  $\mathcal{O}(\xi^4)$  truncation in the smooth matched ansatz (109). Panel (a) shows the UV-matched static potential. The truncated energy is shifted by an additive constant so that it agrees with the exact curve at the shortest plotted separation; the force and local exponent are independent of this convention. Panel (b) shows the force magnitude. The exact branch crosses over from the Coulomb guide  $\kappa/L^2$  to the screened guide  $2\kappa_{\text{RN}}/L^3$ , while the truncated branch approaches the constant wall force in (115). Panel (c) shows the local force exponent  $n_F$ . The exact curve approaches the screened value 3 rather than the linear value 0; the constant-force plateau is a property of the finite polynomial extrapolation.

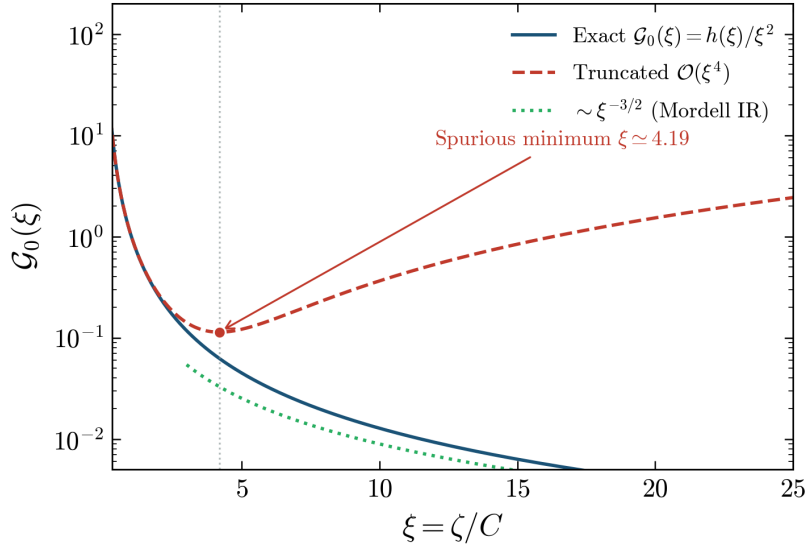


**Figure 8:** The ratio  $\mathcal{G}_0(\xi) \equiv h(\xi)/\xi^2$  on a logarithmic scale, comparing the exact result (solid) to the  $\mathcal{O}(\xi^4)$  truncation (dashed). The dotted line shows the large- $\xi$  asymptotic  $\sim \xi^{-3/2}$ . The truncated series develops a spurious minimum at  $\xi \simeq 4.19$  (circle) followed by polynomial growth, while the exact  $\mathcal{G}_0$  decays monotonically. This demonstrates that strict linear confinement is an artifact of truncation: in the exact throat geometry the rectangular Wilson-loop potential is algebraically screened,  $E(L) \sim -\kappa_{\text{IR}}/L^2$ .

## 5 Outlook

The exact integral representation, the closed  $q/q^*$ -series evaluation, the general- $\Delta$  extension, the variance calculation, the complete-monotonicity/robustness results, and the observable-level force comparison established above open several directions for further work.

For Wilson-loop applications, the main remaining problem is the global matching of  $h(\zeta)$  from the  $\text{AdS}_2$  throat into the full  $\text{AdS}_5$  geometry. The large- $L$  screening established here depends only on the asymptotics of  $h$  deep in the throat,  $h \sim \sqrt{\zeta}$ , and is therefore robust, but a complete description of the quark-antiquark potential at all separations requires an exact or controlled solution for the quantum-corrected warp factor across the entire radial direction. The matching ansatz of [24] provides a starting point, but a first-principles derivation — perhaps using the full spectral decomposition of the Schwarzian sector — would place the intermediate- $L$  regime on the same footing as the infrared.

Within the throat itself, the fully averaged observable  $\langle W[g] \rangle$  — the Schwarzian average of the worldsheet functional, with the connected kernels of (51) evaluated at split arguments — remains the natural step beyond the annealed prescription quantified in Sec. 3.5.

Spatial circular Wilson loops are a natural further application. They require a separate disk boundary-value problem and a controlled perimeter subtraction for the renormalized action, and are left for future work.

A closely related direction is finite temperature. As discussed in Sec. 4.3, a nonzero temperature caps the  $\text{AdS}_2$  throat and should replace the extremal algebraic tail by ordinary thermal screening or disconnected-saddle physics at sufficiently large  $L$ . The remaining technical problem is to carry out the analogous radial reduction of the finite-temperature kernel — now the double-spectral representation of [16, 20], of which the extremal kernel used here is the  $\beta \rightarrow \infty$  limit — and to track how the extremal cancellation  $\Phi(0; \tau) = 0$  (Eq. (32)) is deformed at finite  $\beta$ .

On the string-theory side, the present analysis treats the string semiclassically: classical Nambu–Goto worldsheets in a quantum-corrected background. Both  $\alpha'$  corrections to the worldsheet action and loop corrections from string fluctuations could modify the short-distance coefficients in Eq. (74), and could renormalize the coefficient  $\kappa_{\text{IR}}$  of the infrared tail. However, the  $\sqrt{\zeta}$  scaling of  $h$  is a property of the Schwarzian two-point function [20] and is independent of the worldsheet approximation. The infrared *exponent* in  $E(L) \sim -\kappa_{\text{IR}}/L^2$  — and hence the qualitative screening structure — should therefore be robust under these corrections, even if the coefficient  $\kappa_{\text{IR}}$  itself is not.

The mechanism identified here is not specific to the RN- $\text{AdS}_5$  Wilson-loop setup. In backgrounds where the relevant near-horizon observable reduces to the same Schwarzian two-point kernel [55], the same Mordell-type metric factor appears; whether the monotone decay of the effective string tension persists depends on the behavior of the transverse geometry in the throat. More generally, many near-extremal observables are governed by closely related Schwarzian kernels, including transport properties [25, 26], low-temperature shear correlators and  $\eta/s$ , with regime-dependent conclusions regarding the Kovtun–Son–Starinets bound [27, 28, 31, 32], Hawking radiation spectra from near-extremal rotating black holes [29], quasi-normal mode frequencies [30], and the replica phase structure of the entropy [56]. The precise endpoint asymptotics and modular completions can depend on the operator dimension and observable, but the lesson is common: finite near-boundary or low-temperature

truncations need not remain uniformly valid in the deep throat. Wherever a qualitative conclusion depends on extrapolating such a truncation beyond its controlled regime, an exact-kernel analysis analogous to the one performed here should be possible. When the same metric factor  $h(\zeta)$  enters, the integral representation (15) and the closed  $q/q^*$ -series (43) provide the required check directly.

The general- $\Delta$  subsection suggests a broader mathematical program. We have identified the differential ladders, the integer/half-integer modular dichotomy, the spectral-edge law, and the dimension-dependent nonperturbative scale  $q_\Delta = e^{-\Delta^2 \xi}$ . A full closed Appell–Lerch formula for arbitrary real  $\Delta$  remains open. It would also be interesting to relate the present Mordell/Appell–Lerch structure to the universal Schwarzian sectors in large- $c$  two-dimensional CFTs identified in [20, 55]; establishing a direct connection for the RN-AdS<sub>5</sub> Wilson-loop observable studied here would require a separate derivation.

Finally, the explicit Mordell evaluation suggests a sharper analytic program. Section 3.1 identifies the Borel singularities of the UV expansion at  $t = -\pi^2 k^2$  and relates the first singulant ( $k = 1$ ) to the Mordell scale  $q^* = e^{-\pi^2/\xi}$ . The remaining resurgence problem is to describe the analytic continuation across the negative Borel direction and its relation to the quasi-modular  $E_2$  mixing in (43). The closed  $q/q^*$  representation should also sharpen numerical error estimates at intermediate distances (including the functional form of  $\delta_{\text{mod}}(L)$  in Eq. (74)), where neither the near-boundary Taylor expansion nor the IR power-law tail is adequate. Deep in the throat the  $q = e^{-\zeta/C}$  corrections are exponentially small, and on the large- $L$  string branch, where  $L \propto \zeta_0^{1/4}$ , these become corrections of order  $\exp(-\text{const} \cdot L^4)$  to the algebraic screening tail. Thus the approach to  $E(L) \sim -\kappa_{\text{IR}}/L^2$  is power-law first, with Mordell corrections beyond all orders of the IR  $1/L$  expansion.

## Acknowledgments

We are grateful to Ricardo Espíndola Romero, Jorge Russo, Leonardo Santilli and Joan Simón for correspondence and useful commentary at different stages of this work. Part of this work was carried out while visiting the Centro de Ciencias de Benasque Pedro Pascual, Universidad Complutense de Madrid and Universitat de Barcelona. We thank these institutions for the hospitality. A talk by Jun Nian at the International Congress of Basic Science (ICBS) in Beijing in 2025 provided motivation for some of the developments in this work.

## A Numerical implementation details

This appendix collects the computational specifications underlying Figs. 2–8, in sufficient detail for independent reproduction. All calculations were performed in double-precision floating-point arithmetic ( $\approx 15$ – $16$  significant digits).

### A.1 Evaluation of $h(\xi)$ and $\mathcal{G}_0(\xi)$

The exact metric factor (15),

$$h(\xi) = 2\xi^2 \int_0^\infty dy y^3 e^{-\xi y^2} \coth(\pi y), \quad (\text{A.1})$$

was evaluated by adaptive Gauss-Kronrod quadrature (the `scipy.integrate.quad` routine, which wraps the QUADPACK library [57]). The integrand is smooth on  $(0, \infty)$ ; the factor  $\coth(\pi y)$  has a  $1/y$  singularity at  $y = 0$ , but the product  $y^3 \coth(\pi y) \sim y^2/\pi$  is regular. For numerical stability, the integral was split at  $y = 1$ : on  $[0, 1]$ , we subtracted the  $1/(\pi y)$  piece of  $\coth(\pi y)$  and evaluated the singular part  $\int_0^1 y^2 e^{-\xi y^2}/\pi dy$  analytically (an incomplete gamma function). The remainder and the tail  $[1, \infty)$  were computed by adaptive quadrature. Absolute and relative tolerances were set to  $10^{-12}$ .

*Convergence check.* Increasing the tolerances to  $10^{-14}$  changed  $h(\xi)$  by less than  $10^{-13}$  at all sampled  $\xi \in [10^{-3}, 10^5]$ . The truncation of the upper integration limit was checked by verifying that the Gaussian factor  $e^{-\xi y^2}$  renders the tail contribution below  $10^{-15}$  for  $y > y_{\max}$  with  $y_{\max} = \max(20, 5/\sqrt{\xi})$ .

The confinement indicator  $\mathcal{G}_0(\xi) = h(\xi)/\xi^2$  was obtained by dividing the same integral, and its derivatives (used in checking complete monotonicity numerically) were computed by evaluating the corresponding moment integrals  $(-1)^n \mathcal{G}_0^{(n)}(\xi) = 2 \int_0^\infty y^{3+2n} e^{-\xi y^2} \coth(\pi y) dy$  with the same quadrature scheme.

*Variance evaluation.* The variance (54) was evaluated with the same split quadrature applied to the moments  $\int_0^\infty dy y^{3+2n} e^{-\xi y^2} \coth(\pi y)$ ,  $n = 0, 1, 2$ ; the identity between (53) and the  $\mathcal{G}_0$ -derivative form in (54) was confirmed to 12 digits over  $0.5 \leq \xi \leq 10$ , and the infrared coefficient  $\sqrt{\pi}/3$  to four digits at  $\xi = 10^4$ .

## A.2 Evaluation of the Wilson-loop parametric integrals

The parametric integrals (99)–(100) (throat-only) and the full matched-ansatz integrals (61)–(62) were evaluated as follows.

*Endpoint regularization.* Both integrals develop an integrable square-root singularity at  $u \rightarrow 1^-$  (throat) or  $v \rightarrow 1^+$  (full geometry). This was removed by the substitution  $u = 1 - s^2$  (equivalently  $v = 1 + s^2$ ), which renders the transformed integrand bounded. The regularized integrals were computed by adaptive Gauss-Kronrod quadrature with absolute tolerance  $10^{-10}$  and relative tolerance  $10^{-10}$ .

*Turning-point grid.* For the throat-only computation, 200 values of  $\xi_0$  were spaced logarithmically over  $[10^{-1}, 10^5]$ . For the matched-ansatz computation, 100 values of  $U_0 - U_T$  were spaced logarithmically over  $[10^{-7}, 10^2]$ . At each grid point, the function  $h(\xi)$  was evaluated by the quadrature scheme of Appendix A.1; there is no interpolation table.

*UV cutoff.* The full-geometry integrals were cut off at  $U_{\max} = 10^4$ . The cutoff dependence was checked by repeating the computation at  $U_{\max} = 5 \times 10^3$  and  $U_{\max} = 5 \times 10^4$ : the relative change in the renormalized energy was below  $10^{-6}$  at all sampled turning points.

*Derivative diagnostics.* The stability and concavity conditions (111) involve first and second derivatives of the parametric curve  $(L(U_0), E(U_0))$ . These were computed by centered finite differences on the  $(L, E)$  data:

$$\left. \frac{dE}{dL} \right|_i \simeq \frac{E_{i+1} - E_{i-1}}{L_{i+1} - L_{i-1}}, \quad \left. \frac{d^2E}{dL^2} \right|_i \simeq \frac{(E_{i+1} - E_i)/(L_{i+1} - L_i) - (E_i - E_{i-1})/(L_i - L_{i-1})}{(L_{i+1} - L_{i-1})/2}. \quad (\text{A.2})$$

The logarithmic grid spacing ensures that the fractional step  $\Delta \log(U_0 - U_T) \approx 0.09$  is small enough for the finite-difference quotients to be accurate; doubling the number of grid points to 200 changed the computed signs and local exponents by less than 0.1%.

*Observable force comparison.* For Fig. 7, the force was evaluated directly from the first integral,

$$|F|(U_0) = \frac{U_0^2}{2\pi} \sqrt{f(U_0)h(U_0)}, \quad (\text{A.3})$$

in the same units  $U_T = R = C = 1$  used in the matched-ansatz computation. The exact branch used 150 logarithmically spaced values of  $U_0 - U_T \in [10^{-6}, 10^3]$ . The truncated branch used  $h^{(4)}$  and was sampled as  $U_0 - U_T = (U_{\text{wall}} - U_T) + s$ , with  $s \in [10^{-7}, 10^{2.5}]$  and  $U_{\text{wall}} - U_T = 0.0198806$ . The local exponent  $n_F$  was computed by centered finite differences on  $(\log L, \log |F|)$ . For this plotting-only comparison,  $h(\xi)$  was tabulated on 2000 logarithmically spaced points in  $\xi \in [10^{-8}, 10^8]$  using the equivalent quadrature

$$h(\xi) = \int_0^\infty dx x e^{-x} \coth(\pi \sqrt{x/\xi}), \quad (\text{A.4})$$

and interpolated with a monotone piecewise cubic interpolant [58] in  $(\log \xi, \log h)$ ; direct quadrature spot checks changed the plotted force by less than the line width. The exact energy in Fig. 7(a) was reconstructed by integrating  $dE/dL = |F|$  and fixing the largest- $L$  endpoint to the analytic tail  $E = -\kappa_{\text{RN}}/L^2$ . The truncated energy was shifted by an additive constant to agree with the exact curve at the shortest plotted separation.

*Numerical values.* Table 1 collects the key numerical outputs and their sensitivity to the computational parameters.

Quantity	Value	$U_{\text{max}}$ sensitivity	Grid sensitivity
$(-E_{\text{th}})L_{\text{th}}^2$ ( $\xi_0 > 10^3$ )	0.26003	$< 10^{-5}$	$< 10^{-4}$
$d \log(-E_{\text{th}})/d \log L_{\text{th}}$	-2.001	$< 10^{-3}$	$< 10^{-3}$
$(-E)L^2$ (matched, $\xi_0 > 10^4$ )	$1.804 \times 10^{-3}$	$< 10^{-6}$	$< 10^{-4}$
$d \log(-E)/d \log L$ (matched)	-2.003	$< 10^{-3}$	$< 10^{-3}$
Analytic $\kappa_{\text{th}}$	0.259921	—	—
Analytic $\kappa_{\text{RN}} = \kappa_{\text{th}}/144$	$1.80501 \times 10^{-3}$	—	—

**Table 1:** Key numerical outputs from the rectangular Wilson-loop evaluation and their sensitivity to computational parameters. “ $U_{\text{max}}$  sensitivity” is the relative change when  $U_{\text{max}}$  is varied by a factor of 5. “Grid sensitivity” is the relative change when the number of turning points is doubled.

*Software.* All computations used Python 3.11 with NumPy 1.26 and SciPy 1.12. Plots were generated with Matplotlib 3.8. The source bundle includes `code/reproduce_figures.py`, which exposes the quadrature for  $h(\xi)$ ,  $\mathcal{V}(\xi)$ , the universal throat curve, and the matched force comparison, and reproduces Figs. 4, 5, and 7.

## References

- [1] Juan Maldacena. The Large  $N$  Limit of Superconformal Field Theories and Supergravity, 1998. Adv. Theor. Math. Phys. 2:231–252, arXiv:hep-th/9711200.

- [2] Edward Witten. Anti-de Sitter Space and Holography, 1998. *Adv. Theor. Math. Phys.* 2:253–291, arXiv:hep-th/9802150.
- [3] Juan Maldacena. Wilson Loops in Large  $N$  Field Theories, 1998. *Phys. Rev. Lett.* 80:4859–4862, arXiv:hep-th/9803002.
- [4] Soo-Jong Rey and Jung-Tay Yee. Macroscopic Strings as Heavy Quarks: Large  $N$  Gauge Theory and Anti-de Sitter Supergravity, 2001. *Eur. Phys. J. C* 22:379–394, arXiv:hep-th/9803001.
- [5] Edward Witten. Anti-de Sitter Space, Thermal Phase Transition, and Confinement in Gauge Theories, 1998. *Adv. Theor. Math. Phys.* 2:505–532, arXiv:hep-th/9803131.
- [6] Andrew Chamblin, Roberto Emparan, Gary T. Horowitz, and Robert C. Myers. Charged AdS Black Holes and Catastrophic Holography, 1999. *Phys. Rev. D* 60:064018, arXiv:hep-th/9902170.
- [7] Thomas Faulkner, Hong Liu, John McGreevy, and David Vegh. Emergent Quantum Criticality, Fermi Surfaces, and AdS<sub>2</sub>, 2011. *Phys. Rev. D* 83:125002, arXiv:0907.2694.
- [8] Nabil Iqbal, Hong Liu, and Mark Mezei. Semi-local Quantum Liquids, 2012. *JHEP* 04:086, arXiv:1105.4621.
- [9] Roman Jackiw. Lower Dimensional Gravity, 1985. *Nucl. Phys. B* 252:343–356.
- [10] Claudio Teitelboim. Gravitation and Hamiltonian Structure in Two Spacetime Dimensions, 1983. *Phys. Lett. B* 126:41–45.
- [11] Ahmed Almheiri and Joseph Polchinski. Models of AdS<sub>2</sub> Backreaction and Holography, 2015. *JHEP* 11:014, arXiv:1402.6334.
- [12] Juan Maldacena and Douglas Stanford. Remarks on the Sachdev–Ye–Kitaev Model. *Phys. Rev. D*, 94(10):106002, 2016, arXiv:1604.07818.
- [13] Kristan Jensen. Chaos in AdS<sub>2</sub> Holography, 2016. *Phys. Rev. Lett.* 117:111601, arXiv:1605.06098.
- [14] Juan Maldacena, Douglas Stanford, and Zhenbin Yang. Conformal Symmetry and Its Breaking in Two Dimensional Nearly Anti-de-Sitter Space, 2016. *PTEP* 2016:12C104, arXiv:1606.01857.
- [15] Zhenbin Yang. The Quantum Gravity Dynamics of Near Extremal Black Holes, 2019. *JHEP* 05:205, arXiv:1809.08647.
- [16] Phil Saad, Stephen H. Shenker, and Douglas Stanford. JT Gravity as a Matrix Integral, 2019. arXiv:1903.11115.
- [17] Thomas G. Mertens and Gustavo J. Turiaci. Solvable Models of Quantum Black Holes: A Review on Jackiw–Teitelboim Gravity, 2023. *Living Rev. Rel.* 26(1):4, arXiv:2210.10846.

- [18] Alexei Kitaev and S. Josephine Suh. The Soft Mode in the Sachdev–Ye–Kitaev Model and Its Gravity Dual, 2018. JHEP 05:183, arXiv:1711.08467.
- [19] Douglas Stanford and Edward Witten. Fermionic Localization of the Schwarzian Theory, 2017. JHEP 10:008, arXiv:1703.04612.
- [20] Thomas G. Mertens, Gustavo J. Turiaci, and Herman L. Verlinde. Solving the Schwarzian via the Conformal Bootstrap, 2017. JHEP 08:136, arXiv:1705.08408.
- [21] Thomas G. Mertens. The Schwarzian Theory – Origins, 2018. JHEP 05:036, arXiv:1801.09605.
- [22] Andreas Blommaert, Thomas G. Mertens, and Henri Verschelde. Clocks and Rods in Jackiw–Teitelboim Quantum Gravity. JHEP, 09:060, 2019, arXiv:1902.11194.
- [23] Luca V. Iliesiu and Gustavo J. Turiaci. The Statistical Mechanics of Near-Extremal Black Holes. JHEP, 05:145, 2021, arXiv:2003.02860.
- [24] Xiao-Long Liu, Cong-Yuan Yue, Jun Nian, and Wenni Zheng. Quantum-Corrected Holographic Wilson Loop Expectation Values and Super-Yang-Mills Confinement, 2024. arXiv:2412.11107.
- [25] Xiao-Long Liu, Jun Nian, and Leopoldo A. Pando Zayas. Quantum Corrections to Holographic Strange Metal at Low Temperature, 2024. arXiv:2410.11487.
- [26] Jun Nian, Leopoldo A. Pando Zayas, and Cong-Yuan Yue. Quantum Corrections in the Low-Temperature Fluid/Gravity Correspondence, 2025. arXiv:2510.15411.
- [27] Leopoldo A. Pando Zayas and Jingchao Zhang. One-loop Corrected Holographic Shear Viscosity to Entropy Density Ratio at Low Temperatures, 2025. arXiv:2510.16100.
- [28] Sera Cremonini, Li Li, Xiao-Long Liu, and Jun Nian. Quantum Corrections to  $\eta/s$  from JT Gravity, 2025. arXiv:2510.21602.
- [29] Sabyasachi Maulik, Xin Meng, and Leopoldo A. Pando Zayas. Quantum-Corrected Hawking Radiation from Near-Extremal Kerr–Newman Black Holes, 2026. JHEP 02:205, arXiv:2501.08252.
- [30] Zheng Jiang, Jun Nian, Caiying Shao, Yu Tian, and Hongbao Zhang. Quantum Gravity Corrections to Scalar Quasi-Normal Modes in Near-Extremal Reissner–Nordström Black Holes, 2025. Phys. Rev. D 112:126019, arXiv:2506.22945.
- [31] Blaise Goutéraux, David M. Ramirez, and Clément Supiot. Schwarzian Quantum Corrections to Shear Correlators of the Near-Extremal Reissner–Nordström–AdS Black Hole, 2025. arXiv:2512.19642.
- [32] Marios Kanargias, Elias Kiritsis, Sameer Murthy, Olga Papadoulaki, and Achilleas P. Porfyriadis. Holographic Shear Correlators at Low Temperatures, and Quantum  $\eta/s$ , 2025. arXiv:2512.20443.

- [33] Estia Eichten, Kurt Gottfried, Toichiro Kinoshita, John Kogut, Kenneth D. Lane, and Tung-Mow Yan. Spectrum of Charmed Quark-Antiquark Bound States, 1975. *Phys. Rev. Lett.* 34:369–372.
- [34] E. Eichten, K. Gottfried, T. Kinoshita, K. D. Lane, and T. M. Yan. Charmonium: The Model, 1978. *Phys. Rev. D* 17:3090.
- [35] Gunnar S. Bali. QCD Forces and Heavy Quark Bound States, 2001. *Phys. Rept.* 343:1–136, arXiv:hep-ph/0001312.
- [36] Yoav Kinar, Eliezer Schreiber, and Jacob Sonnenschein.  $Q\bar{Q}$  Potential from Strings in Curved Spacetime – Classical Results, 2000. *Nucl. Phys. B* 566:103–125, arXiv:hep-th/9811192.
- [37] Jacob Sonnenschein. What Does the String/Gauge Correspondence Teach Us About Wilson Loops?, 2000. Lecture notes, arXiv:hep-th/0003032.
- [38] Louis Joel Mordell. The Definite Integral  $\int_{-\infty}^{\infty} \frac{e^{ax^2+bx}}{e^{cx+d}} dx$  and the Analytic Theory of Numbers, 1933. *Acta Math.* 61:323–360.
- [39] Sander P. Zwegers. Mock Theta Functions, 2002. PhD thesis, Universiteit Utrecht, arXiv:0807.4834.
- [40] George E. Andrews and Bruce C. Berndt. Ramanujan’s Lost Notebook, Part V, 2018. Springer.
- [41] Julius Engelsöy, Thomas G. Mertens, and Herman Verlinde. An Investigation of AdS<sub>2</sub> Backreaction and Holography, 2016. *JHEP* 07:139, arXiv:1606.03438.
- [42] Andreas Blommaert, Thomas G. Mertens, and Henri Verschelde. The Schwarzian Theory – A Wilson Line Perspective, 2018. *JHEP* 12:022, arXiv:1806.07765.
- [43] Luca V. Iliesiu, Silviu S. Pufu, Herman Verlinde, and Yifan Wang. An Exact Quantization of Jackiw–Teitelboim Gravity, 2019. *JHEP* 11:091, arXiv:1905.02726.
- [44] Jorge G. Russo, Guillermo A. Silva, and Miguel Tierz. Supersymmetric  $U(N)$  Chern–Simons-Matter Theory and Phase Transitions, 2015. *Commun. Math. Phys.* 338:1411–1442, arXiv:1407.4794.
- [45] Luca Griguolo, Jacopo Papalini, and Domenico Seminara. On the Perturbative Expansion of Exact Bi-Local Correlators in JT Gravity, 2021. *JHEP* 05:140, arXiv:2101.06252.
- [46] R. B. Dingle. Asymptotic Expansions: Their Derivation and Interpretation, 1973. Academic Press.
- [47] G. H. Hardy, J. E. Littlewood, and G. Pólya. Inequalities. Cambridge University Press, 2nd edition, 1952.
- [48] Nadav Drukker, David J. Gross, and Hiroshi Ooguri. Wilson Loops and Minimal Surfaces, 1999. *Phys. Rev. D* 60:125006, arXiv:hep-th/9904191.

- [49] David J. Gross and Hiroshi Ooguri. Aspects of Large  $N$  Gauge Theory Dynamics as Seen by String Theory, 1998. Phys. Rev. D 58:106002, arXiv:hep-th/9805129.
- [50] David V. Widder. The Laplace Transform, 1941. Princeton University Press.
- [51] Raúl E. Arias and Guillermo A. Silva. Wilson Loops Stability in the Gauge/String Correspondence, 2010. JHEP 01:023, arXiv:0911.0662.
- [52] Dimitrios Chatzis. Stability of Wilson Loops and Other Observables in Various Type IIB Backgrounds, 2024. Nucl. Phys. B 1004:116560, arXiv:2401.13637.
- [53] Andreas Brandhuber, Nissan Itzhaki, Jacob Sonnenschein, and Shimon Yankielowicz. Wilson Loops in the Large  $N$  Limit at Finite Temperature. Phys. Lett. B, 434:36–40, 1998, arXiv:hep-th/9803137.
- [54] Mauro Giliaberti, Ali Fatemiabhari, and Carlos Núñez. Confinement and Screening via Holographic Wilson Loops, 2024. JHEP 11:068, arXiv:2409.04539.
- [55] Animik Ghosh, Henry Maxfield, and Gustavo J. Turiaci. A Universal Schwarzian Sector in Two-Dimensional Conformal Field Theories, 2020. JHEP 05:104, arXiv:1912.07654.
- [56] Jun Nian and Yuan Zhong. Replica Phase Transition with Quantum Gravity Corrections, 2026. arXiv:2602.01096.
- [57] Robert Piessens, Elise de Doncker-Kapenga, Christoph W. Überhuber, and David K. Kahaner. QUADPACK: A Subroutine Package for Automatic Integration. Springer, 1983.
- [58] F. N. Fritsch and R. E. Carlson. Monotone Piecewise Cubic Interpolation. SIAM J. Numer. Anal., 17:238–246, 1980.